The Planetary Science Journal, 7:174 (23pp), 2026 July https://doi.org/10.3847/PSJ/ae8258

Geologic History of the Shackleton Crater Region Near the Lunar South Pole: Basis for Future Exploration and Science Activities

Lukas Wueller[1], Yuqi Qian[2], Thomas Frueh[3], James W. Head[4], Wajiha Iqbal[1], Mingyu Tian[2], Antong Gao[1,5], Carolyn H. van der Bogert[1], and Harald Hiesinger[1]
[1] Institut für Planetologie, Universität Münster, Wilhelm-Klemm-Straße 10, 48149 Münster, Germany; lwueller@uni-muenster.de
[2] Department of Earth and Planetary Sciences, The University of Hong Kong, Hong Kong, People's Republic of China
[3] Department of Earth, Environmental, and Planetary Sciences, The University of Tennessee, Knoxville, USA
[4] Department of Earth, Environmental, and Planetary Sciences, Brown University, Providence, RI 02912, USA
[5] Planetary Science Institute, School of Earth and Planetary Sciences, China University of Geosciences, Wuhan, People's Republic of China
Received 2026 April 22; revised 2026 June 11; accepted 2026 June 23; published 2026 July 17

Abstract

The formation of Shackleton crater (~21 km in diameter) represents the last major impact event that reshaped the south polar terrain of the Moon. Because the region is of high interest for future exploration, understanding the regional geology and stratigraphy is critical for selecting scientifically promising landing sites, targeting sample materials, and interpreting obtained samples. Here, we present a new 1:100,000-scale geological map of the region that provides context for several candidate landing sites for the Artemis program and the Chang'e-7 mission. We demonstrate that regional topography, particularly the Shackleton-de Gerlache Ridge, influences the emplacement distance, velocity, and angle of Shackleton ejecta. This controls ejecta thickness and mixing with local materials, leading to significant spatial variability in ejecta thickness and material provenance near candidate landing sites. These effects have direct implications for future landing missions, which will explore materials excavated by the Shackleton impact near the south pole. Combined with the geological context provided by the map, our analysis of ejecta emplacement and distribution provides critical information to help future missions address a variety of key scientific objectives through strategic sampling, and maximize the scientific return from the Shackleton crater region.

Unified Astronomy Thesaurus concepts: The Moon (1692); Planetary geology (2288); Lunar impacts (958)

1. Introduction

Due to its unexplored terrain, diverse geology, proximity to the South Pole–Aitken (SPA) basin, potential volatile resources, and regions that receive prolonged sunlight, the south polar region of the Moon is of high scientific interest for future landing and exploration missions (e.g., National Research Council 2007; NASA 2022a; S. S. Krasilnikov et al. 2023; C. Wang et al. 2024). The ~21 km Shackleton crater is coincident with the south pole, and its formation age is among the youngest large-scale events that have reshaped the region within a few degrees of the south pole. A detailed understanding of the south polar geologic evolution and stratigraphy is essential for mission planning, site selection, science activities, and task-oriented mission support.

To provide this critical information, we mapped the Shackleton crater region near the lunar south pole and investigated how topographic effects influence the emplacement of Shackleton ejecta, thereby controlling ejecta distribution and sample provenance. Our new map extends previous mapping efforts of the adjacent Amundsen crater (L. Wueller et al. 2024) and Mons Malapert–Mons Mouton (L. Wueller et al. 2025) regions. The study region (Figure 1) is near the apparent rim of the SPA basin (e.g., H. Bernhardt et al. 2025; W. Iqbal et al. 2026a), the largest and oldest recognizable basin on the Moon (H. Hiesinger & J. W. Head 2004; I. Garrick-Bethell & M. T. Zuber 2009). The topographically prominent Shackleton-de Gerlache Ridge (SDGR; Figure 1) extends from Shackleton to de Gerlache crater, rises 2.5–3.5 km above the surrounding terrain, and may represent a remnant rim or megablock of the SPA basin (e.g., T. Frueh et al. 2025a; A. J. Gawronska & S. J. Boazman 2025). Thus, the formation of Shackleton crater postdates that of the ridge, but Shackleton formed on top of the ridge, partially destroying and modifying its initial shape and topography. Due to its proximity to the south pole, it has potential volatiles in nearby permanently shadowed regions (PSRs) and favorable illumination conditions for surface exploration (L. Wueller et al. 2026a).

The SDGR is of high interest for both robotic (e.g., China's Chang'e-7 mission, CE-7; Deep Space Exploration Laboratory 2022; G. Wei et al. 2023; C. Wang et al. 2024) and human (e.g., NASA's Artemis program; D. A. Kring et al. 2020a, 2020b, 2020c, 2020d, 2023; NASA 2022b, 2024) surface landing and exploration missions. In the immediate vicinity of Shackleton crater, multiple mission landing sites have been suggested (Figure 2). These include 16 of the 130 candidate landing sites identified within Artemis candidate landing regions across the south polar region (L. Wueller et al. 2026a) that lie on shallow slopes and traversable areas of the continuous Shackleton ejecta deposit mapped in this work. For the CE-7 mission, six potential landing sites have been proposed (Deep Space Exploration Laboratory 2022) on the rim or ejecta deposit of the Shackleton crater.

Here, we present a new geological map of the Shackleton crater region, produced at a mapping scale of 1:100,000, covering ~28,500 km^2. While previous studies have mapped the region at scales of 1:5M (D. E. Wilhelms et al. 1979),

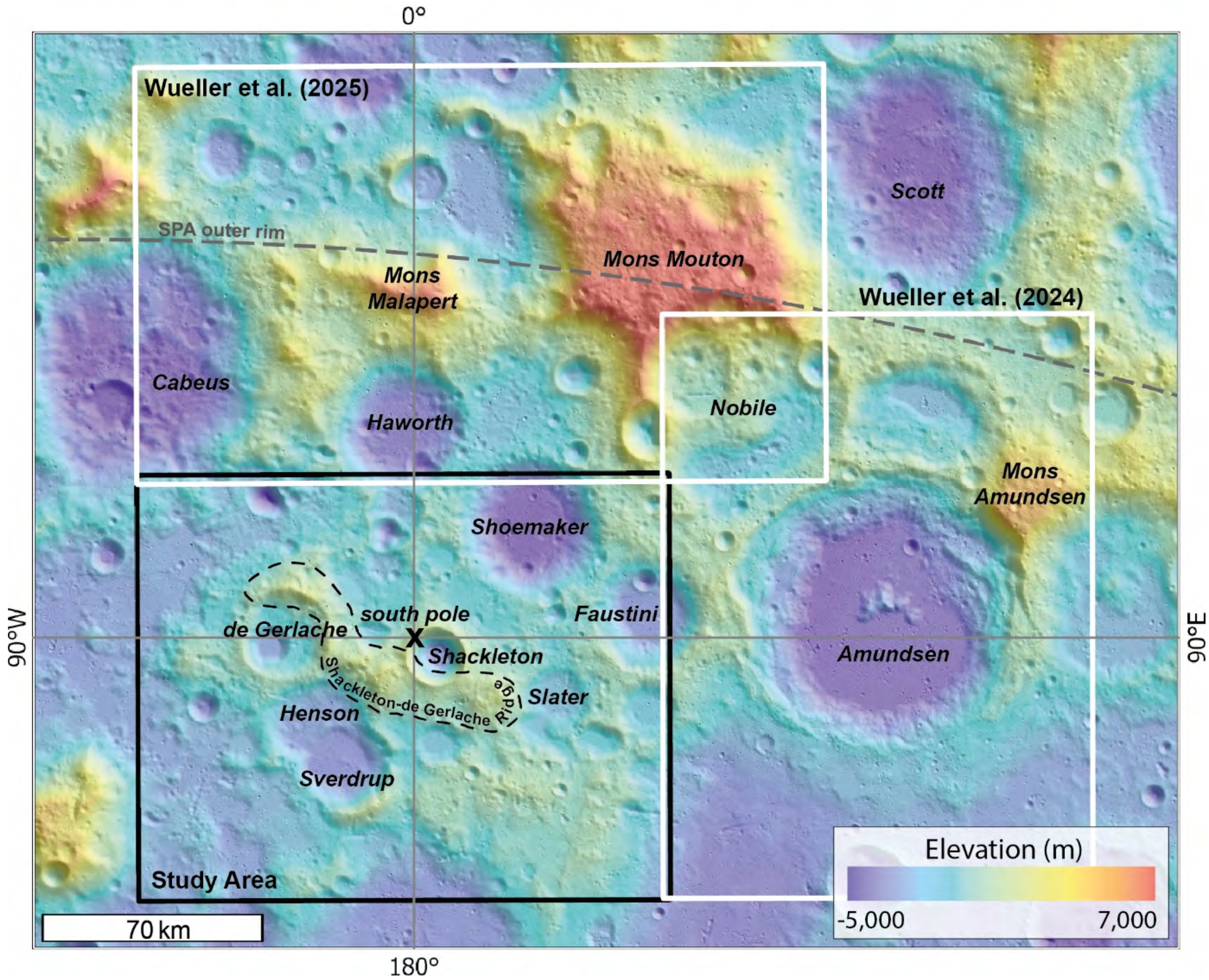

Figure 1. Geographic setting of the lunar south pole with our study area (black box). The white boxes show the extents of the 1:100,000 scale geologic maps of Amundsen crater (L. Wueller et al. 2024) and the Mons Malapert–Mons Mouton region (L. Wueller et al. 2025). The dashed gray line indicates the position of the outer SPA rim (second fit of H. Bernhardt et al. 2025). Figure 1 is displayed on the 20 m pixel^{-1} LRO LDEM topographic base map (M. K. Barker et al. 2023).

1:500,000 (C. Pöhler et al. 2021; W. Iqbal et al. 2026a), 1:300,000 (S. S. Krasilnikov et al. 2023), and 1:250,000 (J. Hostrawser & G. R. Osinski 2025), our 1:100,000 scale mapping is the highest-resolution map of the region to date. H. Bernhardt et al. (2022) mapped parts of the SDGR ("*Connecting Ridge*") at a scale of 1:8,000, providing vital insights for mission and traverse planning. Building on these maps, we provide a regional-scale map that can be integrated with broader regional-to-global maps and landing site-scale maps to link observations made at landing sites with regional or global geologic processes and units (e.g., L. Wueller et al. 2026c). Combining this nested mapping approach (e.g., J. W. Luna et al. 2024; W. Iqbal et al. 2026b) with analyses of the region's spectral properties (see Section 4) and the effects of topography on the distribution and emplacement of Shackleton's ejecta (see Section 5) provides critical information for future landing and sampling missions, including Artemis and CE-7, to maximize their scientific return.

2. Datasets and Methodology

2.1. Datasets

For regional geologic mapping of the Shackleton crater area, we mapped at a scale of 1:100,000 using ESRI's ArcGIS Pro software in south polar stereographic projection and incorporating the following datasets: (a) the Lunar Reconnaissance Orbiter (LRO) Wide Angle Camera (WAC) image mosaic with a spatial resolution of 100 m pixel^{-1} (M. S. Robinson et al. 2010); (b) the LRO Narrow Angle Cameras (NAC) polar mosaics with a spatial resolution of ~1 m pixel^{-1} (M. S. Robinson et al. 2010; B. A. Archinal et al. 2023); and (c) the LRO Lunar Orbiter Laser Altimeter (LOLA) digital elevation models (LDEM) with spatial resolutions of 10 m pixel^{-1} (⩾85°S) and 20 m pixel^{-1} (⩾80°S) (D. E. Smith et al. 2010; M. K. Barker et al. 2023). These DEMs were used to generate hillshade and slope maps with a 20 m baseline, thereby minimizing potential biases caused by variable illumination conditions near the lunar south pole. Additionally, we employed polar spectral maps to study spatial and temporal variations in the spectral properties of surface materials. These include plagioclase and FeO maps derived from Kaguya Spectral Profiler and LOLA data with a spatial resolution of 1 km pixel^{-1} (M. Lemelin et al. 2022a, 2022b), and Moon Mineralogy Mapper (M3) polar plagioclase maps at a spatial resolution of ~193 m pixel^{-1} (K. Du et al. 2026).

2.2. Mapping Technique

Geologic mapping in the south polar region is inherently challenging due to persistently low solar incidence angles, which

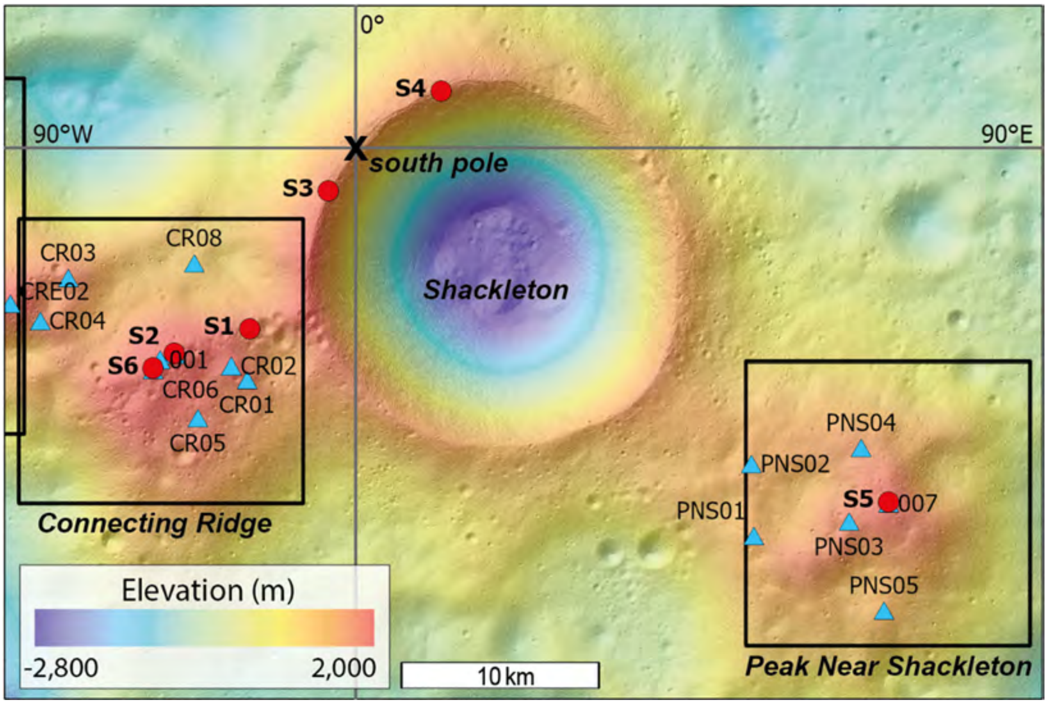

Figure 2. Overview of suggested candidate landing sites near the Shackleton crater, shown on the 20 m pixel^{-1} LRO LDEM topographic base map (M. K. Barker et al. 2023). Black boxes are the two Artemis candidate landing regions "Connecting Ridge" and "Peak Near Shackleton" (NASA 2022b). Candidate landing sites proposed for the CE-7 mission are shown in red (Deep Space Exploration Laboratory 2022), and potential Artemis landing sites are shown as blue triangles (L. Wueller et al. 2026a, 2026b).

produce extensive shadowing from high-relief topography (E. Mazarico et al. 2011) and limit image-based geologic mapping. To ensure uniform mapping criteria and scale throughout the study area, we derived artificially illuminated hillshade maps at different azimuths using LOLA topography data (M. K. Barker et al. 2023). These hillshade maps served as a base map and allowed for consistent identification and characterization of landforms and unit boundaries, using various illumination geometries. Additional topographic context was provided by LOLA DEMs and slope maps derived at 10 m pixel^{-1} spatial resolution (M. K. Barker et al. 2023). These were primarily used to assess surface morphology and crater degradation states, indicative of the stratigraphic position of the mapped units. We employed image datasets from LRO WAC and NAC (M. S. Robinson et al. 2010; B. A. Archinal et al. 2023) to evaluate surface texture and morphology. Spectral data were used only for unit interpretation and were thus not specifically applied to the mapping.

To ensure consistency and readability on a regional scale, the mapping technique and geologic units are based on previous mapping efforts of the adjacent Amundsen crater (L. Wueller et al. 2024) and Mons Malapert–Mons Mouton regions (L. Wueller et al. 2025) (Figure 1). Consequently, the mapping was performed at a scale of 1:100,000, and the final map plate was exported at a scale of 1:300,000 in A0 format. Geologic contacts were delineated based on morphological, structural, and stratigraphic relationships, using hillshade and slope maps, image data, and topographic datasets. Contacts that could be confidently located were mapped as *certain*, whereas gradational or obscure contacts whose locations could not be identified with confidence were mapped as *approximate*. All features $\geqslant$5 km in extent are included on the map, while smaller features were omitted at the mapping scale. We modified the chronostratigraphy originally proposed by D. E. Wilhelms et al. (1987) and later updated by G. Neukum & B. A. Ivanov (1994) to better resolve the relative age relationships within the predominantly pre-Nectarian terrain. We assessed relative age relationships using crater degradation, the apparent density of superposed primary craters, and stratigraphic relationships, such as superposition, cross-cutting, and embayment (e.g., J. W. Head 1975; T. W. Offield & H. A. Pohn 1970). To ensure comparability with previous maps (e.g., D. E. Wilhelms et al. 1979; P. D. Spudis et al. 2008; S. S. Krasilnikov et al. 2023; L. Wueller et al. 2024, 2025), we follow the symbology, standards, and recommendations of the Planetary Geologic Mapping Protocol (J. A. Skinner et al. 2022) and the Federal Geographic Data Committee (FGDC 2006). The nomenclature conforms to that of the Gazetteer of Planetary Nomenclature.[6]

3. Geologic Map

The largest impact crater within the study area is Shoemaker crater (∼52 km diameter), whereas the ∼21 km diameter Shackleton crater formed directly at the lunar south pole. The geology of the study region is dominated by pre-Nectarian materials, which are represented by six mapped geologic units (Figure 3). Younger materials within the area are predominantly associated with impact-related processes that have modified the region since the pre-Nectarian period.

3.1. Description and Interpretation of Map Units

3.1.1. Pre-Nectarian Massifs—pNm

Pre-Nectarian massifs are characterized by their positive topographic prominence relative to their surrounding regions. In the study area, the Shackleton-de Gerlache Ridge (SDGR)

[6] https://planetarynames.wr.usgs.gov/

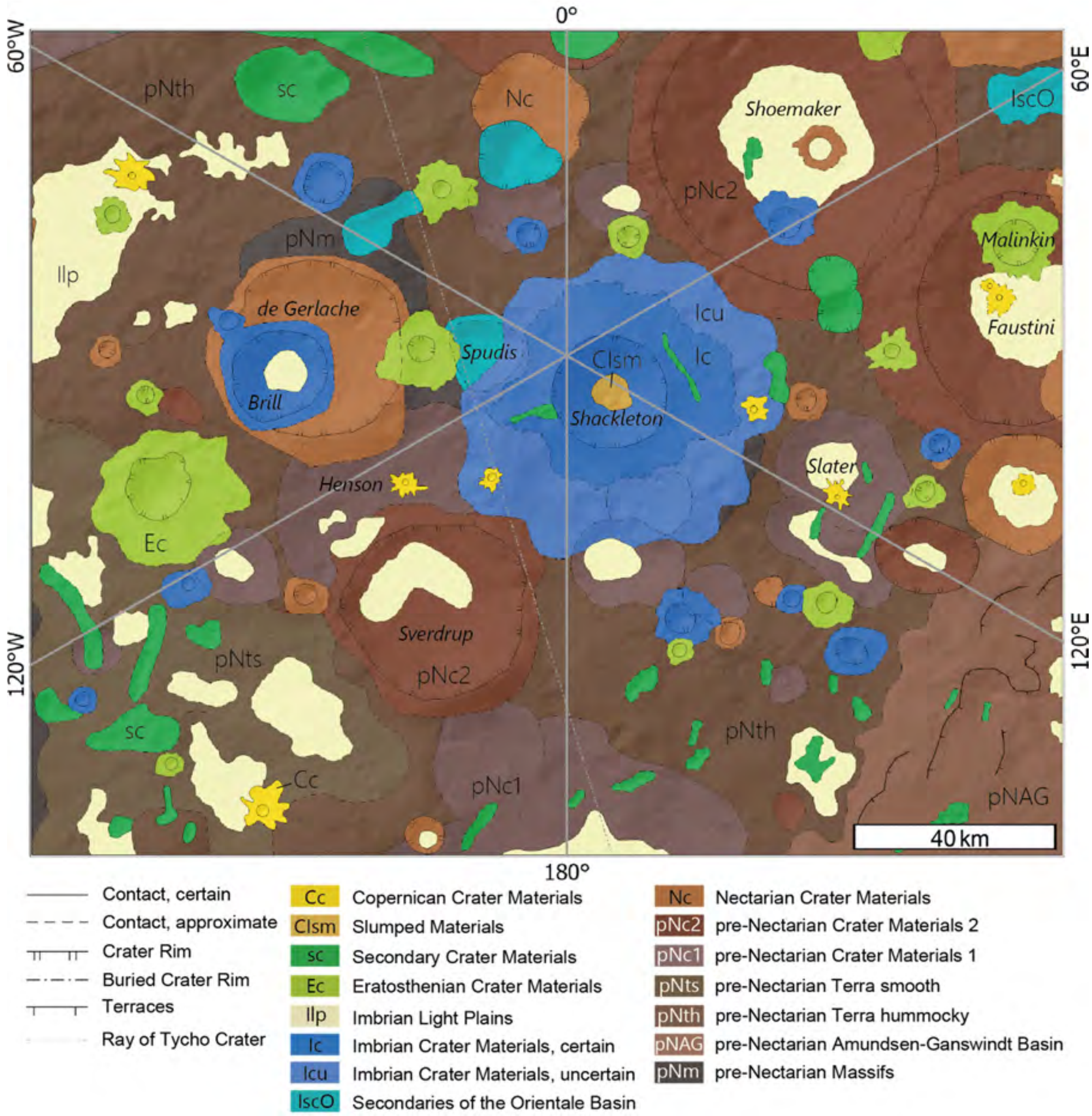

Figure 3. Geologic map of the Shackleton crater region near the lunar south pole produced at a mapping scale of 1:100,000 and exported at a scale of 1:1.25M on a 20 m pixel^{-1} LDEM hillshade base map (M. K. Barker et al. 2023).

rises 2.5–3.5 km above the surrounding terrain. The SDGR extends approximately 100 km from the Nectarian-aged de Gerlache crater to the Imbrian-aged Shackleton crater and possibly beyond, crossing the lunar south pole (Figure 3). The slopes on the flanks of the SDGR can be as steep as 30° and average at about 15°. The section of the ridge that connects the ∼31 km diameter de Gerlache and ∼21 km diameter Shackleton craters is often referred to as the "Connecting Ridge" (e.g., NASA 2022b).

Interpretation: The SDGR is intersected and superposed by younger impact craters and their ejecta materials, such as de Gerlache, Marvin, and Shackleton craters. The exposed portions of the SDGR are mapped as *pNm* units, whereas the hatched overlay indicates the covered but topographically exposed portions of the ridge (Figure 3). The ridge's pre-Nectarian age, inferred from its degradation state and superposition relationships with younger features, is consistent with previous maps and studies (e.g., D. E. Wilhelms et al. 1987; P. D. Spudis et al. 2008; S. S. Krasilnikov et al. 2023; A. J. Gawronska & S. J. Boazman 2025). The SDGR is considered part of the inner ring of the ancient SPA basin (e.g., P. D. Spudis et al. 2008; I. Garrick-Bethell & M. T. Zuber 2009; S. S. Krasilnikov et al. 2023), indicating that the massifs once extended beyond this region (A. J. Gawronska & S. J. Boazman 2025). Subsequent impact cratering determined the massif's current extent and exposed SPA-related lithologies at the surface. Alternatively, the massif that defines the SDGR is a crustal megablock associated with the SPA basin formation (T. Frueh et al. 2025a) or a remnant rim structure of an ancient impact crater that formed after the SPA basin. In any case, the resulting lithologies likely persist within the SDGR and have been excavated by younger impacts, such as those that formed de Gerlache and Shackleton craters.

3.1.2. Pre-Nectarian Amundsen–Ganswindt Basin—pNAG

The ∼380 km diameter Amundsen–Ganswindt basin (∼81.5°S; 125.7°E) is located between the lunar south pole and the Schrödinger basin (e.g., G. A. Neumann et al. 2015; L. Wueller et al. 2024; J. Hostrawser & G. R. Osinski 2025). While much of the basin has been altered or buried by subsequent impacts, such as the formation of Schrödinger basin, a segment of its rim structure remains within the study area (Figure 3). This arcuate segment features an elevation change of ∼3 km, linear slope breaks that are parallel to the curvature of the rim, and a high degree of overall degradation.

Interpretation. This unit is interpreted as the remnant rim of the pre-Nectarian Amundsen–Ganswindt basin, which was estimated to be ∼4.26 Ga old (C. Orgel et al. 2018). Since the peak ring of the Amundsen–Ganswindt basin is mostly destroyed, only a few arcuate segments of the initial peak ring structure remain (J. Hostrawser & G. R. Osinski 2025). These segments were intersected by younger impacts, such as the Imbrian-aged Idel'son L crater (L. Wueller et al. 2024). The observed linear slope breaks are interpreted as degraded basin wall terraces, which, like the entire unit, were modified by the deposition of younger ejecta material from nearby impact events, resulting in their degraded appearance. Due to the proximity of the Amundsen–Ganswindt basin to the south pole, it is likely that the region contains a large amount of the basin's ejecta that was redistributed by subsequent gardening impacts (e.g., T. Frueh et al. 2025a).

3.1.3. Pre-Nectarian Terra Hummocky and Smooth—pNth and pNts

The majority of the study area is dominated by pre-Nectarian terra material, which fills the intercrater plains. We distinguish between hummocky (*pNth*) and smooth (*pNts*) materials based on their morphology. The *pNth* unit exhibits a rugged appearance with an attenuated morphology that incorporates subdued, discontinuous, arcuate fragments. The *pNth* unit has an average slope of 8°.7 ± 4°.4, which is steeper and more heterogeneous than the *pNts* unit (6°.4 ± 3°.2). The *pNts* unit has a similar degree of degradation, but shows a more attenuated and subdued morphology. Both endmembers of the terra unit are overlain by crater and plains material ranging in age from the pre-Nectarian to Copernican (Figure 3).

Interpretation. The undivided crater and basin material of the hummocky and smooth pre-Nectarian terra units consist of heavily degraded fragments of ancient impact structures. These impact materials are no longer recognizable and are partially buried by material from subsequent impacts. This includes local craters such as de Gerlache, Henson, Sverdrup, and Shackleton craters, as well as basins in proximity to the south pole, such as Amundsen–Ganswindt, Ashbrook, and Schrödinger. As described by D. E. Wilhelms et al. (1987), S. S. Krasilnikov et al. (2023), and L. Wueller et al. (2024, 2025), the rugged and attenuated morphology is the result of the mixing of locally derived debris with ejecta from these nearby craters and basins. The arcuate but discontinuous fragments likely represent eroded crater rims that resisted erosion and burial by subsequent processes (e.g., H. Hiesinger & k. Tanaka 2020). Consequently, the pre-Nectarian terra material incorporates highly degraded and segmented crater and basin structures, local ejecta and debris, and basin ejecta. The smooth terra material likely comprises a higher proportion of ejecta and/or less-preserved fragments of ancient structures, resulting in its more subdued topography.

3.1.4. Pre-Nectarian Crater Materials 1 and 2—pNc1 and pNc2

Following the classification scheme introduced by L. Wueller et al. (2025), craters were categorized based on their degree of degradation (J. W. Head 1975; N. Agarwal et al. 2019; J. Wang et al. 2020), modifying the chronostratigraphic framework of D. E. Wilhelms et al. (1987). Since the study area is dominated by pre-Nectarian materials (Figure 3), pre-Nectarian craters were further subdivided into two degradation classes: a more degraded pre-Nectarian crater 1 unit (*pNc1*) and a comparatively less degraded pre-Nectarian crater 2 unit (*pNc2*). These classes are distinguished by a combination of quantitative and qualitative criteria, including crater wall slopes, crater rim continuity, overall crater preservation, and superposition relationships. Craters assigned to the *pNc1* unit are characterized by comparatively shallow wall slopes of <15° (Figure 4(F)), discontinuous and degraded rims, and a greater degree of superposition and infilling by younger materials. Conversely, *pNc2* craters exhibit steeper circumferential wall slopes exceeding 15° (Figure 4(E)), more continuous and better-preserved rims, and are locally superimposed on *pNc1* craters (Figure 3). Representatives of the *pNc1* unit include Henson and Slater craters, whereas Faustini, Shoemaker, and Sverdrup exemplify the *pNc2* class.

Interpretation. Due to the high level of degradation, extensive modification and infilling by subsequent processes, as well as their superposition relationship with the surrounding units, both *pNc1* and *pNc2* classes are interpreted as pre-Nectarian in age (D. E. Wilhelms et al. 1987). Craters assigned to the pNc1 unit are considered older than those of the *pNc2* unit. This is indicated by their shallower crater wall slopes and greater rim and wall discontinuity. Both units have experienced modification through impact cratering and mixing with ejecta deposits; however, these effects are more pronounced in the older *pNc1* craters. Crater diameter shows no systematic relationship with either crater class and spans a wide range, from a diameter of ∼52 km (Shoemaker crater) to several craters with diameters of ∼10 km. Crater size–frequency distribution measurements by A. R. Tye et al. (2015) yield model ages of 4.10 ± 0.03 Ga for Faustini crater and 4.15 ± 0.02 Ga for Shoemaker crater, both mapped as part of the younger *pNc2* unit (Figure 3), suggesting that craters of the *pNc1* unit are older than at least ∼4.15 Ga.

3.1.5. Nectarian Crater Materials—Nc

Impact craters assigned to this category are highly degraded but retain partially recognizable ejecta deposits and crater rims in topographic data. Although most craters are circular in shape, some exhibit irregular morphologies, such as de Gerlache crater (∼31 km diameter), which formed on the topographically high SDGR. Craters of this class superpose pre-Nectarian units, yet are themselves partially buried by younger materials emplaced during the Imbrian, Eratosthenian, and Copernican periods.

Interpretation. Based on their high level of degradation (e.g., T. W. Offield & H. A. Pohn 1970; J. W. Head 1975; J. Wang et al. 2020) and their superposition by younger (crater) materials, these craters are interpreted to be Nectarian in age (D. E. Wilhelms et al. 1987). Their crater floors are partially

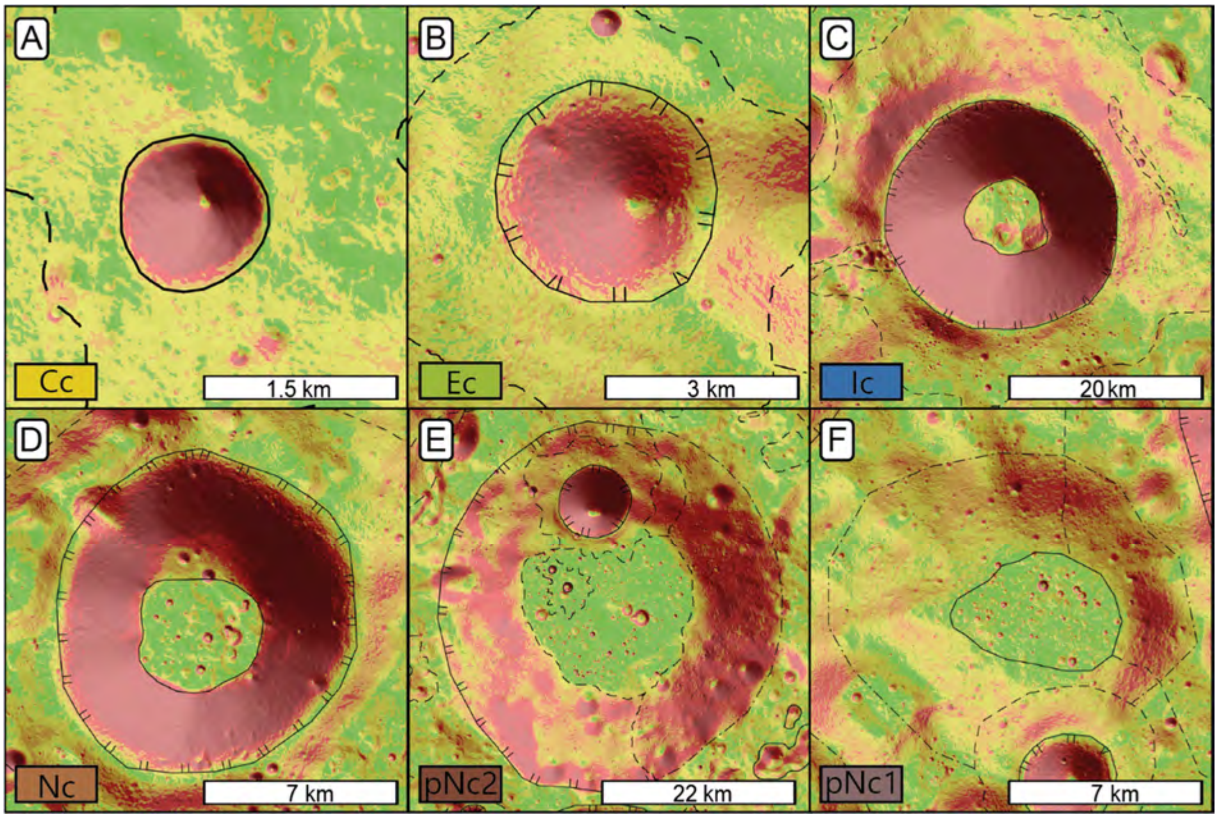

Figure 4. Examples of crater classes spanning the (a) Copernican, (b) Eratosthenian, (c) Imbrian, (d) Nectarian, and (e), (f) pre-Nectarian periods. The 10 m pixel^{-1} slope maps (M. K. Barker et al. 2023) are shown on a 10 m pixel^{-1} hillshade base map. Green colors indicate slopes of <5°, yellow symbolizes slopes of 5°–10°, orange shows slopes of 10°–15°, red indicates slopes of 15°–20°, and wine-red colors symbolize slopes >20°. Shackleton crater is shown in panel (c) and Faustini crater in panel (e).

filled with younger materials, including ejecta from nearby impact events and plains materials (Figure 4(D); L. Qiao et al. 2024). This interpretation is consistent with previous maps (e.g., D. E. Wilhelms et al. 1979; S. S. Krasilnikov et al. 2023; L. Wueller et al. 2024, 2025).

3.1.6. Imbrian Crater Materials, Certain and Imbrian Crater Materials, Uncertain—Ic and Icu

Impact craters in this category display an intermediate level of degradation and are partially superposed by material from younger units (i.e., *Ec* or *Cc*). Compared to younger craters, they are characterized by a more subdued topography, nearly circular shapes, and raised rims. Their crater floors are often flat, and some are covered by plains-forming materials (*Ilp*; e.g., Brill crater). Continuous ejecta deposits are topographically and morphologically discernible in the vicinity of the crater but progressively diminish with increasing distance from the rim until they transition into the discontinuous ejecta deposit. For this reason, we distinguish between *certain* (*Ic*) and *uncertain* ejecta materials (*Icu*). The latter unit is applied only for the distal ejecta materials of the ~21 km diameter Shackleton crater (Figure 4(C)), whose distal ejecta materials are more challenging to delineate compared to the proximal ejecta materials. This is likely to be related to the illumination conditions near the south pole (e.g., E. Mazarico et al. 2011). Consequently, the *uncertain* ejecta extent was mapped based on hillshade data, whereas NAC image data was considered for mapping Shackleton's *certain* ejecta deposit.

Interpretation. We attributed these crater materials to the Imbrian period based on their morphologic characteristics, superposition relationships, and intermediate degree of degradation (e.g., T. W. Offield & H. A. Pohn 1970; J. W. Head 1975; D. E. Wilhelms et al. 1987). The largest Imbrian crater in the study area, Shackleton crater at the lunar south pole, has been variously classified as Imbrian by T. Frueh et al. (2025a), S. S. Krasilnikov et al. (2023), P. D. Spudis et al. (2008), and M. T. Zuber et al. (2012), and as Eratosthenian by B. Giuri et al. (2024), J. Hostrawser & G. R. Osinski (2025), and D. E. Wilhelms et al. (1979). We classify Shackleton crater as Imbrian, as the continuous ejecta deposit is challenging to delineate and is extensively overprinted by numerous superposed craters ranging from hundreds of meters to kilometers in diameter. Both units, *Ic* and *Icu*, are interpreted to be part of Shackleton crater's continuous ejecta deposit. Furthermore, crater size–frequency distribution analyses by D. A. Kring et al. (2021), A. R. Tye et al. (2015), P. D. Spudis et al. (2008), and M. T. Zuber et al. (2012) yield model ages of 3.43 +0.038 −0.051 Ga, 3.51 +0.05 −0.08 Ga, 3.6 ± 0.4 Ga, and 3.69 +0.02 −0.03 Ga, respectively, for Shackleton crater. These age estimates support a formational age of Shackleton crater in the Imbrian period.

3.1.7. Imbrian Light Plains—Ilp

Isolated patches of light plains are scattered throughout the study area and are preferentially concentrated in topographic depressions, particularly on the floors of Faustini and Shoemaker craters (Figure 3). These plains form laterally extensive, flat surfaces with an average slope of 4°.6 ± 3°.8 and are characterized by smooth, relatively featureless morphologies. Individual light plains deposits vary considerably in size, ranging from small patches of ∼10 km^2 to extensive deposits such as the ∼500 km^2 plain within Shoemaker crater. The light plains overlie (pre-)Nectarian units and some Imbrian craters, and are themselves superposed by small impact craters of Eratosthenian and Copernican ages.

Interpretation. The distribution and stratigraphic relationships of the light plains suggest emplacement after major impact events formed and modified the region through the end of the Nectarian period. We interpret these deposits as resulting from basin-forming and local impact events, potentially associated with the formation of the Orientale and Schrödinger basins (e.g., H. M. Meyer et al. 2020; B. Giuri et al. 2024; L. Qiao et al. 2024).

3.1.8. Slumped Materials—CIsm

The floor of Shackleton crater is characterized by a rugged, hummocky texture with mounds up to ∼250 m high. The surface slopes of the floor materials are irregular and up to 20°, with a clear slope break to the inner wall of Shackleton crater. The floor is sparsely cratered, with craters less than ∼400 m in diameter. Slumping and accumulation of debris on the floor also occurs in other craters, but they are too small to be mapped at our scale.

Interpretation. We interpret the floor deposit in Shackleton crater as resulting from material slumping downslope from the inner crater wall, creating landslides and accumulating debris on the crater floor. Boulders are concentrated along the slope break between the crater wall and floor (S. J. Boazman et al. 2022; A. J. Gawronska & S. J. Boazman 2025), indicating downslope material transport. Because the inner crater wall and the slumped floor material are sparsely cratered, we suggest that landslides recently altered the floor of Shackleton crater. This is further evidenced by the secondary crater chain (*sc*) on the SDGR that abruptly ends on the Shackleton crater rim and does not extend into its interior, likely implying that mass-wasting modified the crater's floor (H. Bernhardt et al. 2022) and is still episodically active (P. Mahanti et al. 2025). The slumping is likely triggered by the instability of steep wall slopes (P. Mahanti et al. 2025).

3.1.9. Eratosthenian Crater Materials—Ec

Impact craters assigned to this category are circular and predominantly bowl-shaped, with intact, raised crater rims and diameters ranging from ∼2.5 to ∼12 km within the study area (Figure 4(B)). They feature a circumferential ejecta deposit marked by finely textured ridges and lobes, indicative of a low degree of degradation (J. W. Head 1975). Within the study area, the Malinkin crater (∼8.5 km diameter) and Marvin crater (∼5 km diameter) are the only formally named examples of this crater class. They occur on pre-Nectarian, Nectarian, and Imbrian units.

Interpretation: Owing to their well-preserved morphology, superposition relationships, and low degree of degradation, these craters are interpreted to be Eratosthenian in age (D. E. Wilhelms et al. 1987).

3.1.10. Copernican Crater Materials—Cc

This unit consists of small impact craters with diameters of less than ∼2.5 km, characterized by fresh and sharply defined morphologies (Figure 4(A)), and prominent bright radial rays that are visible in image data. Their continuous ejecta deposits display well-defined ridges and grooves, reflecting a very low degree of degradation (e.g., J. W. Head 1975; N. Agarwal et al. 2019). These craters are not superposed by other geologic units.

Interpretation. Based on their well-preserved morphology and the presence of bright radial rays, these impact craters are classified as Copernican in age (D. E. Wilhelms et al. 1987).

3.1.11. Secondary Crater Materials—sc

Craters that occur in clusters or linear chains are classified as secondary craters. These craters are elongated and irregular in shape, often overlapping, and typically exhibit a comparable degree of degradation within individual chains or clusters (e.g., V. R. Oberbeck & H. R. Aggarwal 1977; A. S. McEwen & E. B. Bierhaus 2006). In the study area, secondary crater chains range in length from ∼5 to ∼35 km. Secondary craters are superposed on units spanning different stratigraphic periods, from pre-Nectarian to Imbrian materials (Figure 3). While no clear orientation pattern is apparent, several chains show a general NE–SW alignment (top-right to bottom-left of the map area).

Interpretation. Chains and clusters of small, irregularly shaped craters are interpreted as secondary craters of undetermined ages, with the exception of Orientale secondaries, which were mapped separately (see below). For the NE–SW-oriented chains, Schomberger crater represents a potential source, while Wiechert J crater may be responsible for some of the shorter chains toward the lunar farside (toward the bottom of the map). Moreover, an ejecta ray from the Copernican-aged Tycho crater is visible in Mini-RF data (C. M. Dundas & A. S. McEwen 2007; E. G. Rivera-Valentín et al. 2024) and crosses the study area in an NW–SE direction (Figure 3).

3.1.12. Secondaries of the Orientale Basin—IscO

One group of secondary crater clusters that can be distinguished from the others are those related to the formation of the Orientale basin. The study region records three secondary clusters of the Orientale basin, with craters up to ∼15 km in diameter, which includes Spudis crater located near the south pole. All clusters show a similar degree of degradation and are oriented toward the Orientale basin on a regional-to-global scale (e.g., D. E. Wilhelms et al. 1979; D. Guo et al. 2018).

Interpretation. Based on their size and radial orientation relative to the Orientale basin (D. Guo et al. 2018), these secondary clusters are attributed to the formation of the ∼930 km diameter Orientale basin ∼3.81 Ga ago in the Imbrian period (C. Orgel et al. 2018). Due to the size of the basin, ejected material following ballistic trajectories traveled far enough to produce recognizable secondary chains and clusters at considerable distances from the parent basin (Orientale basin is ∼2500 km away from the south pole). The Orientale secondaries mapped are consistent with previous studies and maps (e.g., D. E. Wilhelms et al. 1979; D. Guo et al. 2018; S. S. Krasilnikov et al. 2023).

3.2. Stratigraphy of Map Units

Based on superposition and cross-cutting relationships, apparent relative degradational stages and crater densities, and derived model ages from previous studies (e.g., P. D. Spudis et al. 2008; M. T. Zuber et al. 2012; A. R. Tye et al. 2015; D. A. Kring et al. 2021; S. S. Krasilnikov et al. 2023; B. Giuri et al. 2024; L. Wueller et al. 2024, 2025), we

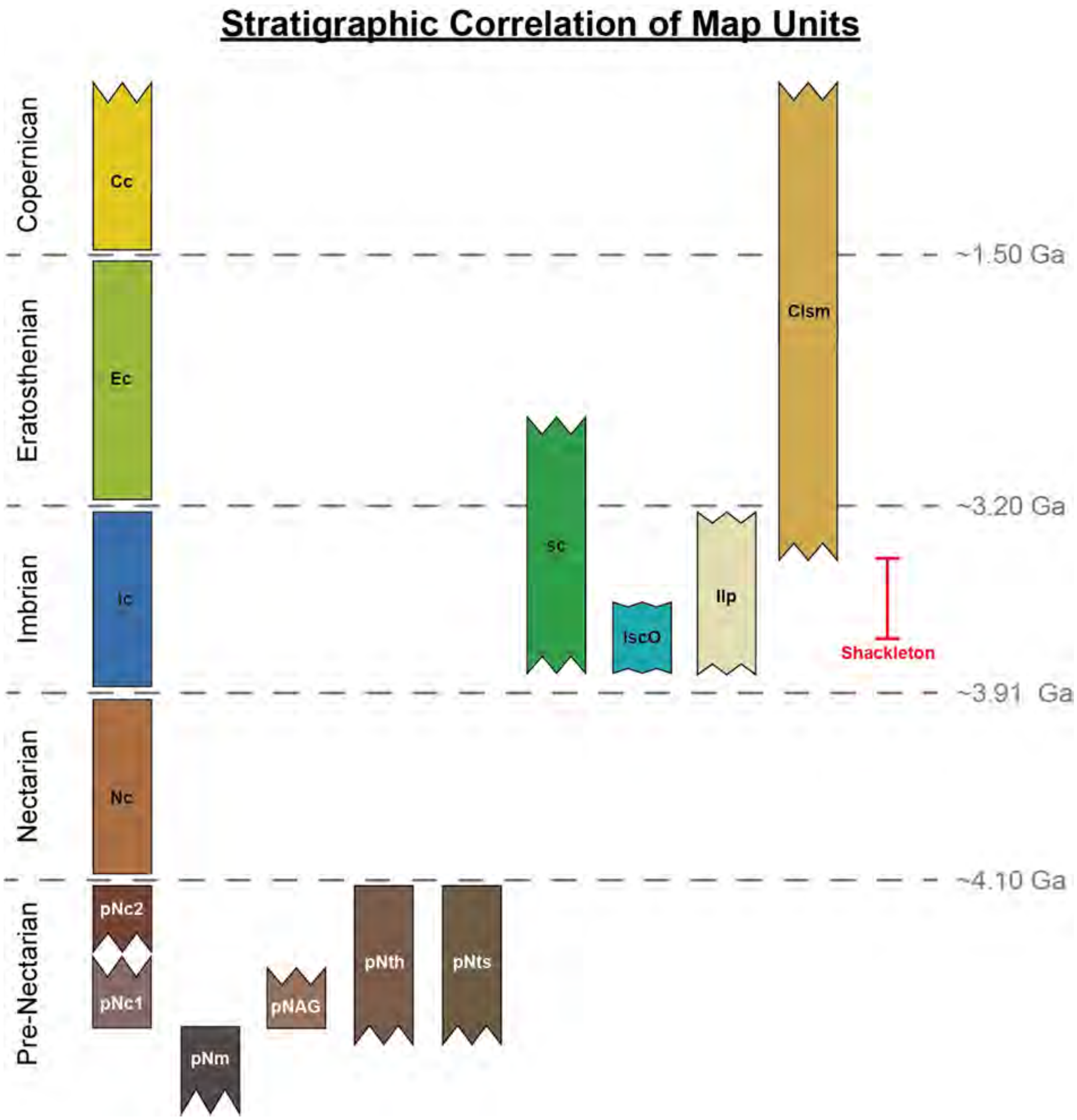

Figure 5. Stratigraphic correlation chart of mapped units. Absolute period extents are adopted from G. Neukum & B. A. Ivanov (1994), who modified the stratigraphic scheme originally proposed by D. E. Wilhelms et al. (1987), as described by H. Hiesinger et al. (2023) and H. Hiesinger & K. Tanaka (2020). The range of ages for Shackleton crater were derived by D. A. Kring et al. (2021), P. D. Spudis et al. (2008), A. R. Tye et al. (2015), and M. T. Zuber et al. (2012).

constructed a stratigraphic correlation chart of mapped units (Figure 5).

The correlation chart shows that most of the units formed during the pre-Nectarian period and are related to the formation of the SPA basin between ∼4.23 and 4.33 Ga (H. Takeda et al. 2006; H. Hiesinger et al. 2012; V. A. Fernandes et al. 2013; I. Garrick-Bethell et al. 2020; K. H. Joy et al. 2025; B. Su et al. 2025; L. Wueller et al. 2025), the Amundsen–Ganswindt basin at ∼4.26 Ga (C. Orgel et al. 2018), and local impact craters, including the Faustini, Henson, Slater, and Sverdrup craters. The formation of these craters redistributed and mixed pre-existing SPA and Amundsen–Ganswindt ejecta materials and potentially the underlying primordial crust, depending on the thickness of SPA ejecta in the region (T. Frueh et al. 2025a; see their Figure 11). Continued impact cratering reworked and modified the original (crater) materials, resulting in their erosion and burial that formed the region's terra deposits (*pNth* and *pNts*). Since the end of the pre-Nectarian period (∼4.1 Ga ago; G. Neukum & B. A. Ivanov 1994), geologic activity has decreased, resulting in fewer and smaller impact craters from the Nectarian throughout the Copernican period. During the Imbrian period, the region was modified by secondary craters originating from the Orientale basin and by the emplacement of light plains (*Ilp*), which are potentially associated with the formation of the Orientale and Schrödinger basins (e.g., H. M. Meyer et al. 2020; B. Giuri et al. 2024; L. Qiao et al. 2024). Between ∼3.43 Ga and ∼3.69 Ga (P. D. Spudis et al. 2008; M. T. Zuber et al. 2012; A. R. Tye et al. 2015; D. A. Kring et al. 2021), the ∼21 km diameter Shackleton crater formed at the lunar south pole on the Shackleton-de Gerlache ridge. Its floor is likely to have been resurfaced episodically by downslope slumping of material and boulders that have been liberated from the steep inner crater wall (e.g., H. Bernhardt et al. 2022; A. J. Gawronska & S. J. Boazman 2025; P. Mahanti et al. 2025). The formation of Shackleton crater marked the last major cratering event in the study region. Since then, all units have been modified by subsequent smaller impacts or distal ejecta and secondary craters from larger distant craters. This includes the deposition of ray material from Tycho crater, located ∼1400 km away, crossing the ejecta deposit of Shackleton crater (Figure 3; C. M. Dundas & A. S. McEwen 2007; E. G. Rivera-Valentín et al. 2024).

4. Spectral Characteristics of the Mapped Region

To assess regional compositional characteristics and mineralogic variation, we examined spectral datasets from Kaguya's Spectral Profiler (J. Haruyama et al. 2008; M. Lemelin et al. 2022a, 2022b), the Moon Mineralogy Mapper (M3; R. O. Green et al. 2011; D. P. Moriarty & N. E. Petro 2024; K. Du et al. 2026), and the Lunar Prospector (D. J. Lawrence et al. 2002).

The Kaguya Spectral Profiler acquired hyperspectral observations (500–2600 nm wavelength) of the lunar surface (J. Haruyama et al. 2008). By calibrating Kaguya gridded reflectance data (∼500–1550 nm) to absolute reflectance values obtained by LOLA at 1064 nm, M. Lemelin et al. (2022a) derived quantitative polar mineral maps (low-Ca-pyroxene, high Ca-pyroxene, olivine, and plagioclase) with a spatial resolution of 1 km pixel^{-1} and an uncertainty of 9 wt%. M3 spectral data provide the highest spatial resolution currently available (140–280 m pixel^{-1}) for the polar regions, resulting in regional mosaics of ∼1.5 km pixel^{-1} (D. P. Moriarty & N. E. Petro 2024), and, when combined with LOLA reflectance data, enable processing quantitative mineral maps of the south polar region at ∼193 m pixel^{-1} spatial resolution (K. Du et al. 2026). Prospector Fe abundance maps provide a spatial resolution of 0.°5 pixel^{-1} and an uncertainty of <0.5% for neutron count rates near the poles (D. J. Lawrence et al. 2002).

The SPA basin is characterized by a gradual decrease in FeO content, ranging from ∼15 wt% near the apparent center of the SPA basin to ∼5 wt% in the anorthositic feldspathic highlands on the lunar nearside (B. L. Jolliff et al. 2000). Since our study area is near the expected rim of the SPA basin, the average FeO abundance is intermediate at 7.1 ± 1.2 wt% with a local minimum poleward of ∼87°S (Figure 6(A)). Furthermore, plagioclase is abundant (Figure 6(B)) and indicates anorthositic norite/troctolite (60–77.5 wt% plagioclase) and noritic/troctolitic anorthosite (77.5–90 wt% plagioclase) regolith compositions (D. Stöffler et al. 1980; M. Lemelin et al. 2022a; T. Frueh et al. 2025a).

The Kaguya SP polar spectral maps (M. Lemelin et al. 2022b) reveal locally low FeO abundances of 5.6 ± 0.7 wt% (Figure 6(A)) and high plagioclase abundances of 81.3 ± 1.1 wt% (Figure 6(B)) in the Shackleton crater and its ejecta deposit. These observations indicate a localized noritic/troctolitic anorthosite composition associated with the Shackleton crater (D. Stöffler et al. 1980). Some pixels in the Kaguya plagioclase maps are indicative of pure anorthosite (PAN) lithologies (S. Yamamoto et al. 2012), with a plagioclase content exceeding 90 wt%, the highest plagioclase abundances within the mapped area (M. Lemelin et al. 2022a). However, the relatively coarse spatial resolution of the Kaguya maps (1 km pixel^{-1}) limits detection to either extremely pure or laterally extensive anorthositic exposures (e.g., T. Frueh et al. 2025a). The low FeO and high plagioclase abundances detected by Kaguya, as well as the location of Shackleton crater on the SDGR (which likely represents uplifted crust or a crustal megablock associated with the formation of the SPA basin; e.g., A. J. Gawronska et al. 2020; T. Frueh et al. 2025a), suggest that the Shackleton crater may have excavated material of crustal composition (e.g., A. J. Gawronska et al. 2020; D. P. Moriarty & N. E. Petro 2024; T. Frueh et al. 2025a). The excavation of anorthositic crustal material was also suggested for Amundsen crater, whose central peak exhibits similar low FeO and high plagioclase abundances (L. Wueller et al. 2024).

Redistribution of this material within Shackleton's ejecta likely resulted in the elevated plagioclase signal observed by the Kaguya Spectral Profiler (M. Lemelin et al. 2022a), consistent with ejecta thinning and a decreasing anorthositic signal with increasing distance from the crater (D. P. Moriarty & N. E. Petro 2024). Furthermore, stratigraphic excavation models suggest that the Shackleton impact penetrated an SPA ejecta deposit up to ∼1.2 km thick, potentially exposing underlying anorthositic crustal material (T. Frueh et al. 2025a). Given Shackleton's Imbrian age (e.g., P. D. Spudis et al. 2008; M. T. Zuber et al. 2012; A. R. Tye et al. 2015; D. A. Kring et al. 2021) and its high plagioclase abundance (Figure 6(B)), its ejecta deposit is likely to be enriched in mafic-free lithologies and crustal components relative to older terrains that were more extensively modified by subsequent impacts.

However, the anorthositic signature identified in Kaguya mineral maps (M. Lemelin et al. 2022a) is not confirmed by M3 data, which show absorption bands inconsistent with mafic-free anorthosite (D. P. Moriarty & N. E. Petro 2024). Furthermore, Lunar Prospector Gamma Ray Spectrometer Fe and Kaguya Spectral Profiler FeO data show contrasting spatial distributions near the south pole. Lunar Prospector data indicate a smooth regional gradient from higher to lower Fe concentrations from inner to outer SPA structures across the south pole (D. J. Lawrence et al. 2002), while Kaguya Spectral Profiler records a local minimum around Shackleton crater (Figure 6(A)). D. P. Moriarty & N. E. Petro (2024) suggested that the discrepancy may stem from variations in the two instruments' sensing depth, spatial resolution, or Fe specification. Iron present in oxides or glasses would elevate Lunar Prospector Fe measurements without producing strong absorption features in reflectance spectra (D. P. Moriarty & C. M. Pieters 2018), resulting in low FeO abundances in Kaguya data. Additionally, the high-relief topography and high albedo of the south polar region may bias spectral abundance estimates (D. P. Moriarty & N. E. Petro 2024). Recent mineral maps derived from M3 data (K. Du et al. 2026) show improved spatial correspondence with Kaguya detections of high plagioclase concentrations in Shackleton's ejecta and PAN exposures along its rim (e.g., S. Yamamoto et al. 2012; J. Haruyama et al. 2013). L. Hood et al. (2026) suggested that swirls (bright, optically immature surface features shielded from space weathering by localized magnetic anomalies) may be present near the south pole, based on a strong magnetic anomaly that spatially overlaps with high surface albedo.

Despite these spectral uncertainties, Shackleton crater and its associated materials remain primary targets for sampling primordial crust (D. P. Moriarty & N. E. Petro 2024; T. Frueh

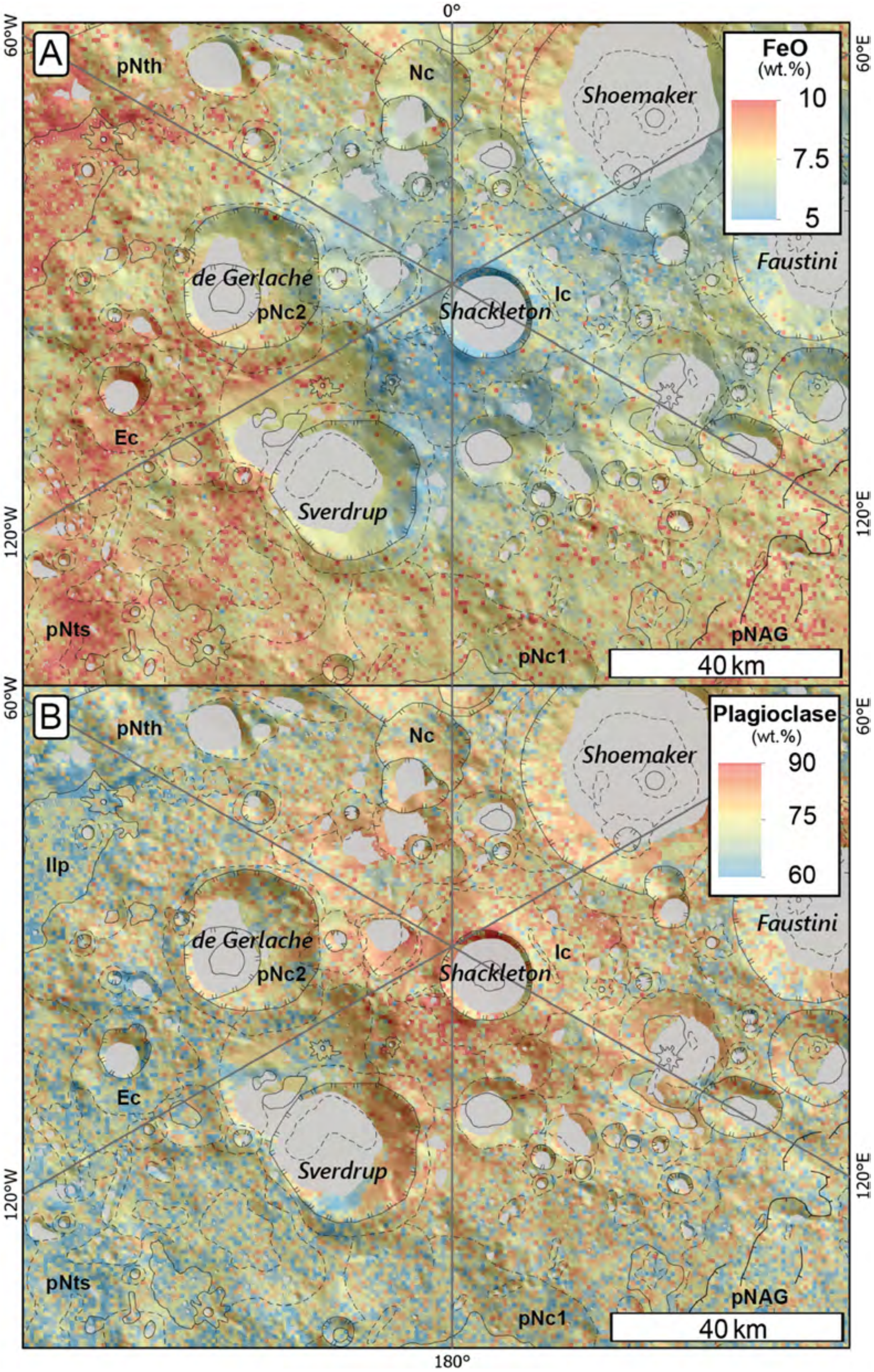

Figure 6. Distribution of (A) FeO and (B) plagioclase based on 1 km $pixel^{-1}$ spectral data with a 9 wt% uncertainty from M. Lemelin et al. (2022b) on a hillshade base map. Mapped unit boundaries and crater rims (Figure 3) are included to show the characteristics of the mapped units. Spectral data are unavailable in PSRs (M. K. Barker et al. 2023, gray areas).

et al. 2025a). Its ejecta deposit contains abundant boulders and outcrops, offering access to coherent lithologies (H. Bernhardt et al. 2022; S. J. Boazman et al. 2022). Even if the anorthositic signal in the Kaguya data proves to be (partially) a misinterpretation, Shackleton's geological context and relatively young age still support the presence of crustal components in its ejecta. As emphasized by D. P. Moriarty & N. E. Petro (2024), in situ investigations and sampling are

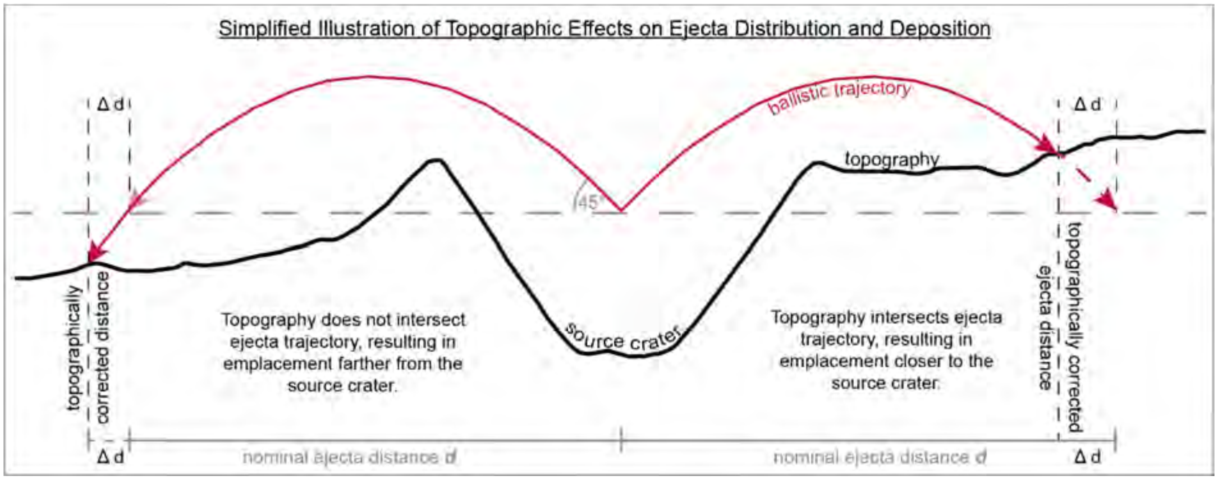

Figure 7. Schematic cross section of a crater, with ejecta deposition at lower (left part) and higher (right part) elevations compared to flat terrain. Lower topography results in ejecta being emplaced farther from the crater, whereas higher topography intercepts the excavated ejecta closer to the crater. Note that this is a simplified representation, as ejection angles and launch positions evolve with crater formation time. Instead, ejecta are launched from progressively increasing radial distances within the transient crater during crater formation (e.g., E. M. Shoemaker 1960; D. E. Maxwell 1977; K. A. Holsapple & R. M. Schmidt 1987).

essential to resolving spectral ambiguities and determining whether Shackleton's ejecta preserves substantial abundances of primordial crust material, for example, using the Lunar Raman Spectrometer on board CE-7 (C. Wang et al. 2024).

5. Topographic Effects on the Distribution of Shackleton Ejecta

The surrounding topography determines how far ejecta can travel once excavated from its parent crater, as well as its velocity upon emplacement (e.g., V. R. Oberbeck 1975; D. A. Kring 2025; T. Frueh & D. A. Kring 2026a). Higher topography, e.g., a massif, intercepts predicted ballistic ejecta trajectories (e.g., T. Frueh & D. A. Kring 2026a), resulting in ejecta being emplaced closer to the source crater than on flat terrain and potentially the formation of ballistic shadows, regions where ejecta is absent or reduced in thickness due to the influence of topography (right part of Figure 7). Conversely, lower topography results in the emplacement of ejecta at greater distances from the source crater than one would observe on flat terrain (left part of Figure 7). Consequently, the surrounding topography plays a critical role in the depositional mechanisms of the ejecta, influencing its time of flight, kinetic energy, emplacement angle, and emplacement velocity (D. A. Kring 2025; T. Frueh & D. A. Kring 2026a). These factors determine the degree of vertical mixing with local material and the degree of lateral transport across the surface during ballistic ejecta emplacement, which leads to thickening and thinning of deposited ejecta. This directly influences the stratigraphy and provenance of south polar samples and should be considered for future surface missions (T. Frueh & D. A. Kring 2026a). Therefore, we analyzed the effects of the formation of Shackleton crater on the topographically prominent SDGR, focusing on the ejecta extent (Section 5.1), thickness distribution (Section 5.2), as well as emplacement velocities and mixing (Section 5.3).

5.1. Shackleton Ejecta Extent

We followed the methodology described and applied by T. Frueh & D. A. Kring (2026a, 2026b) to construct trajectories of ejecta emplaced within the continuous ejecta deposit. We use π-group scaling to constrain ejecta launch positions from the transient crater that evolve with crater formation time (e.g., D. E. Maxwell 1977; K. R. Housen et al. 1983; K. A. Holsapple & R. M. Schmidt 1987; H. J. Melosh 1989). For impact on flat surfaces, experiments and modeling show that ejection launch angles are initially high and decrease with crater formation time, ranging from ∼55° to ∼35° for impact angles between 90° and 45° (e.g., D. E. Maxwell 1977; P. H. Schultz & D. E. Gault 1985; M. J. Cintala et al. 1999; J. L. B. Anderson et al. 2003). Here, we adapted an ejection angle of 45° (M. J. Cintala et al. 1999; S. H. Halim et al. 2021) but provide error ranges for estimated ejecta extents using ejection angles of 35° and 55° (Tables A1 and A2). Ejection velocity decreases with increasing ejection time; consequently, material launched early from near the crater center travels farther than material ejected later from closer to the transient crater rim (e.g., D. E. Maxwell 1977; K. R. Housen et al. 1983; K. A. Holsapple & R. M. Schmidt 1987; H. J. Melosh 1989). We only show trajectories corresponding to the emplacement of the continuous ejecta deposit (Figure 8). The minimum and maximum extents of the continuous ejecta deposit are given by Equation (1) (H. J. Moore et al. 1974):

$$R_{ce} = \quad 2.348^{+0.564}_{-0.454} * \quad R_c{}^{1.006}. \tag{1}$$

For this equation, R_{ce} is the radius of the continuous ejecta deposit, and R_c is the crater radius. We calculated minimum, nominal, and maximum ejecta deposit extents based on the error of $2.348^{+0.564}_{-0.454}$. We utilized the 500 m pixel^{-1} LOLA DEM (D. E. Smith et al. 2010) for topographic information and modeled ejecta trajectories in MATLAB R2024a.

On a planar surface, the maximum extent of the continuous ejecta deposit is ∼31 km from the crater center (H. J. Moore et al. 1974; Shackleton's diameter is 21 km). Here, we consider ballistic trajectories of ejecta that lands at the outer edge of the continuous ejecta deposit of Shackleton crater, but since ejecta spreads out upon emplacement, such trajectories do not necessarily contribute directly to the continuous ejecta deposit. Accounting for topographic effects near Shackleton crater shows that high topography (e.g., near landing site *001*) intercepted ballistic ejecta trajectories,

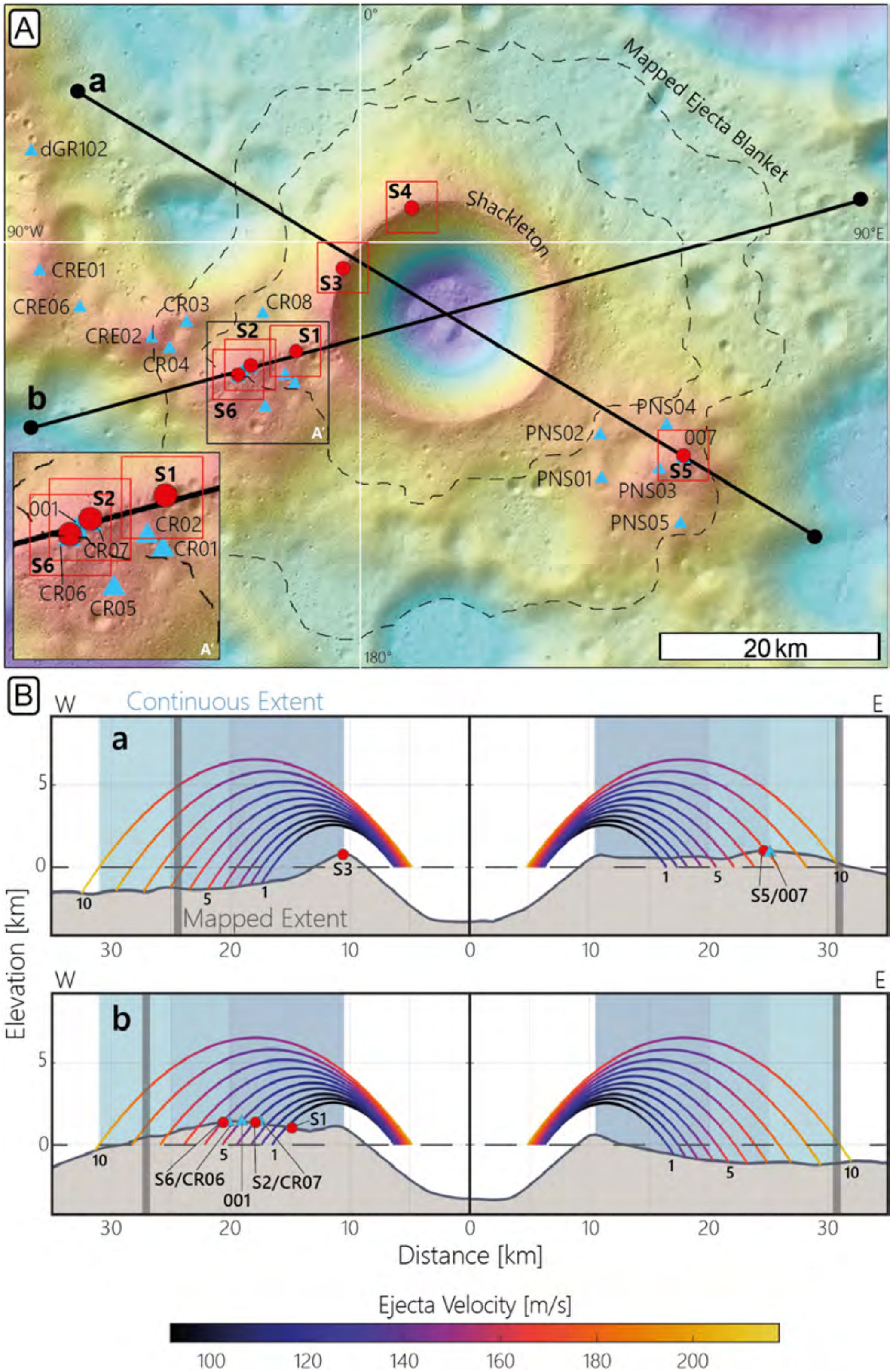

Figure 8. (A) Topographic map of Shackleton crater (20 m pixel^{-1}; M. K. Barker et al. 2023) with the mapped ejecta deposit (Figure 3) and locations of potential landing sites for the CE-7 mission (red circles; Deep Space Exploration Laboratory 2022) and the Artemis campaign (blue triangles; L. Wueller et al. 2026a). (B) Ejecta trajectories for a 45° ejection angle and launch positions moving toward the transient crater rim. The shaded blue areas represent the shortest (lighter hue), nominal, and maximum (darker hue) continuous ejecta deposits (H. J. Moore et al. 1974). Trajectories are colored by ejecta velocity and numbered from 1 to 10 with distance from the crater rim. Vertical gray lines indicate the morphologically mapped ejecta extent (2.5× vertical exaggeration).

resulting in emplacement 1.58 km (∼15%; +0.50 km/−0.72 km; Table A2) closer to the rim of the Shackleton crater than expected for flat terrain (trajectory 5 (west) in Figure 8(B)). In contrast, lower topography extended trajectories, leading to ejecta emplacement 1.47 km (∼7%; +0.52 km/−0.40 km; Table A2) farther from the Shackleton crater are compared to a

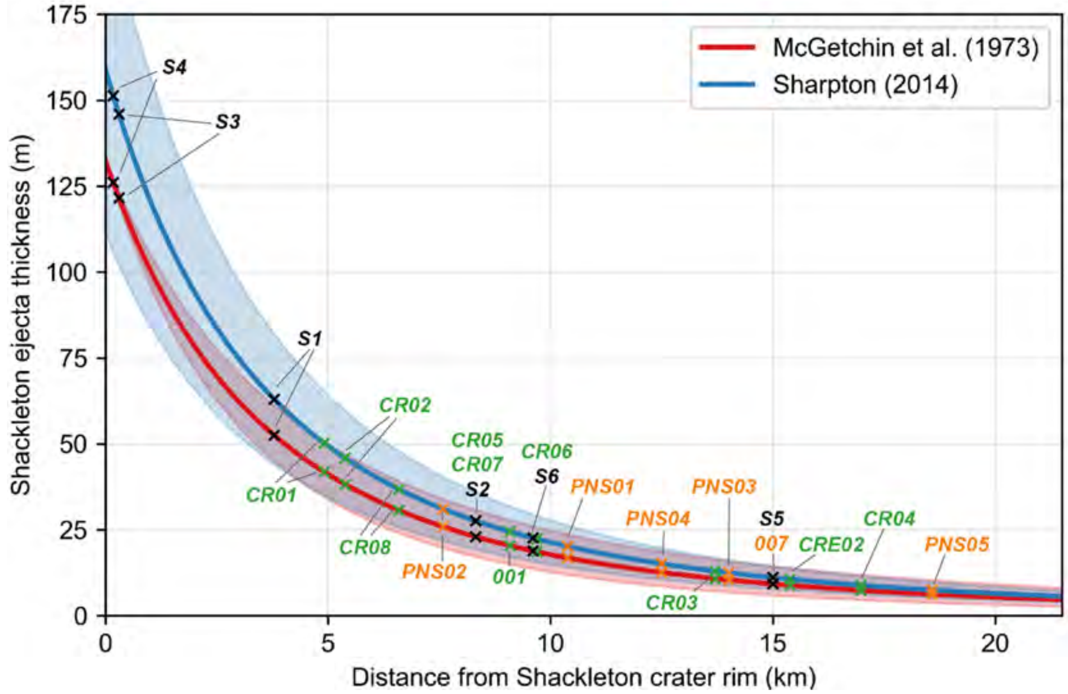

Figure 9. Estimated Shackleton ejecta thickness as a function of distance from the crater based on scaling models of T. R. McGetchin et al. (1973) and V. L. Sharpton (2014). Shaded areas indicate the error range inherent to Equations (2) and (3). The error calculation for T. R. McGetchin et al. (1973) was later introduced by H. J. Melosh (1989). Black marks indicate the locations of the six CE-7 candidate landing sites (Deep Space Exploration Laboratory 2022), orange marks represent Artemis candidate landing sites in the "Peak Near Shackleton" region (L. Wueller et al. 2026a), and green marks indicate Artemis candidate landing sites in the "Connecting Ridge" region (L. Wueller et al. 2026a). Their respective thicknesses are included in Tables 1–3 and are discussed in Section 6.

flat pre-impact topography scenario (trajectory 10 (west) in Figure 8(B)). This results in localized extension and shortening of the ejecta deposit as a function of underlying topography.

The maximum extent of the ejecta deposit can be greater on low topography and reduced over high topography. This is supported by the morphologically mapped extent of the Shackleton ejecta deposit (Figure 3, vertical gray lines in Figure 8(B)), which is largely consistent with the estimated maximum extent of the continuous Shackleton crater ejecta deposit (blue shaded area in Figure 8(B)). The largest discrepancy occurs along the western part of profile A toward Spudis crater, where the mapped ejecta extent falls several kilometers short of the estimated extent (Figure 8(B)), possibly due to pre-existing topography or the impact direction of the Shackleton-forming impactor. However, ejecta degradation over time introduces uncertainty to the mapped extent, and the original continuous ejecta deposit may have extended beyond currently mapped boundaries.

5.2. Shackleton Ejecta Thickness Distribution

Several scaling models have been developed to estimate the thickness of the ejecta deposit (d) as a function of the crater's radius (R_c) and distance from the crater (r_d). We used the scaling relationships of T. R. McGetchin et al. (1973), who derived the first scaling relationship for lunar craters based on nuclear test craters and small impact craters on Earth (Equation (2)), and V. L. Sharpton (2014), who remotely investigated the topography of lunar craters ranging from 2–45 km in diameter (Equation (3)). With a diameter of 21 km, Shackleton crater is in the transitional range from simple-to-complex craters (e.g., H. J. Melosh 1989). All units are in meters:

$$d = 0.14^{*} \quad R_c{}^{0.74*}(r_d/R_c)^{-3.0} \quad {}^{(\pm 0.5)} \tag{2}$$

$$d = 3.95(\pm 1.19)^{*} \quad R_c{}^{0.399*}(r_d/R_c)^{-3.0} \quad . \tag{3}$$

Generally, both scaling models are in good agreement with each other, especially when considering the model uncertainties (shaded areas in Figure 9). For the distal parts of the continuous ejecta deposit of Shackleton crater, differences in the estimated thicknesses are small, while the discrepancy increases closer to the crater rim. This may be related to the consideration of structural rim uplift by V. L. Sharpton (2014), which is a major component of raised crater rims, with only 20% of the rim material being actual excavated ejecta. Furthermore, we note that more scaling models exist that can estimate the ejecta thickness of lunar craters and basins (e.g., R. J. Pike 1974; K. R. Housen et al. 1983; K. A. Holsapple 1993; C. I. Fassett et al. 2011). However, these were either conceptual models tested through impact experiments, or were derived or only tested for impact events larger than the 21 km diameter Shackleton crater, such as the Imbrium or Orientale basins. Therefore, we limit our analysis to the T. R. McGetchin et al. (1973) and V. L. Sharpton (2014) models that are widely used to scale the thickness of a crater's ejecta deposit to its diameter (e.g., T. Frueh et al. 2025a; A. S. Krasilnikov et al. 2024). The existing models could be tested with the lunar ground-penetrating radar on CE-7, which has detection depths of >40 and 400 m for its high- and low-frequency channels, respectively (C. Wang et al. 2024).

These two models indicate that the continuous ejecta deposit around Shackleton crater thins with increasing distance from the crater (Figure 10(A)), decreasing from ∼132 to ∼4 m

(T. R. McGetchin et al. 1973) and from ∼159 to ∼5 m (V. L. Sharpton 2014). However, this assumes flat pre-impact topography, which is not the case, as previously discussed. Therefore, we produced another map based on local relief, qualitatively illustrating where topographic effects may have led to thicker or thinner ejecta deposits relative to a flat scenario (Figure 10(B)). For instance, ejecta accumulates near the base of slopes facing the Shackleton crater, resulting in thicker ejecta deposits, due to slower uphill flow compared to spreading over a flat surface (T. Frueh & D. A. Kring 2026a). In contrast, ejecta emplaced on steep slopes facing away from Shackleton crater is transported downslope, resulting in thinner ejecta on the slope and accumulation at its base (Figure 10(C)). Consequently, the steep slopes surrounding the SDGR likely have thinner ejecta than predicted by a planar scenario (Figure 10(B)). Generally, the steeper the slope, the more downslope slumping occurs, producing a much thinner ejecta deposit relative to that predicted by scaling relationships. Conversely, the bases of Shackleton-facing slopes and topographic lows, such as those within Spudis crater, accumulated ejecta, yielding thicker deposits (Figure 10(B)). Because ejecta emplacement was not significantly modified by the shallow slopes between Shackleton and Shoemaker craters, we anticipate nominal ejecta thickness in this region that is comparable to the estimations using Equations (2) and (3) (Figure 10).

5.3. Shackleton Ejecta Emplacement and Mixing

In addition, regional topography influences the emplacement angle and speed of excavated ejecta materials by intercepting or extending ballistic trajectories, modifying the mixing process between ejecta and local materials (Figure 7; T. Frueh & D. A. Kring 2026a). This will directly influence the composition and provenance of samples collected from the Shackleton ejecta deposit. Thus, we investigated areas where the emplacement speed of Shackleton ejecta was higher or lower due to topographic effects (Figures 8(B), 11(A)). This reveals that in areas with higher topography than Shackleton crater itself, ejecta emplacement velocities are lower. On the other hand, lower topography near Haworth, Henson, Shoemaker, and Sverdrup craters led to extended trajectories with increased acceleration. This resulted in higher ejecta emplacement speeds compared to those estimated for flat terrain (Figure 11(A)). Additionally, higher emplacement speeds tend to result in more mixing with local materials (e.g., V. R. Oberbeck et al. 1975), whereas slower-than-nominal emplacement is expected to result in less mixing. The degree of mixing during ejecta emplacement is also determined by the emplacement velocity, which influences the amount of kinetic energy induced into the subsurface. Generally, emplacement velocities increase with distance from the crater (Figure 8(B)). When massifs intercept ballistic trajectories, the ejecta is accelerated by gravitational pull for a shorter period of time than in a flat terrain scenario. This likely results in reduced emplacement velocities (Figures 8(B), 11(A)) and reduced mixing of the ejecta with local materials. Conversely, where low-lying topography elongates ballistic trajectories and extends the time of gravitational acceleration, emplacement velocities increase (Figures 8(B), 11(A)). These effects may have led to increased mixing with local materials and ejecta spreading upon emplacement.

We estimated the mixing factor (μ) for Shackleton ejecta emplacement following V. R. Oberbeck (1975) and V. R. Oberbeck et al. (1975):

$$\mu = 0.0183^{*} \quad {r_d}^{0.87}, \tag{4}$$

where r_d is the distance of the location of interest to the center of Shackleton crater (measured in kilometers). The mixing factor provides the ratio of local to ejecta material (V. R. Oberbeck 1975; V. R. Oberbeck et al. 1975), with higher values indicating more mixing, and lower values indicating less mixing during ejecta emplacement. This shows that mixing with local materials increases with increasing distance from the crater (Figure 11(B)), reflecting the increase in ejecta impact velocities at greater distances. Near the Shackleton crater rim, ∼14% of the surface material is local regolith incorporated into the ejecta. In contrast, local regolith accounts for ∼38% of the material near the edge of the continuous ejecta deposit (Figure 11(B)). However, based on provenance studies of Apollo 16 regolith, N. E. Petro & C. M. Pieters (2006) suggest that Equation (4) overestimates the μ parameter by a factor of 2. Thus, the abundance of local material in the Shackleton ejecta deposit may be smaller than indicated in Figure 11(B). Regardless of the uncertainty of the mixing factor, Shackleton ejecta remained the dominant component of the deposited material, but the ejecta fraction decreases with increasing distance from the crater.

By comparing the estimated mixing factor for Shackleton ejecta with emplacement angles and velocities, we evaluate whether topographic variations have resulted in less or more mixing with local materials than anticipated for flat terrain (V. R. Oberbeck 1975; V. R. Oberbeck et al. 1975). We predict increased mixing where emplacement speeds are higher, e.g., within Spudis crater, yielding higher local-to-ejecta material ratios in regolith samples. Conversely, we suggest that higher fractions of Shackleton ejecta are present atop the SDGR because ejecta emplacement was lower velocity (Figure 11(A)), leading to reduced mixing effects. Consequently, the ratio of local to ejecta material may decrease in any regolith samples collected from this region. Thus, samples will likely contain a higher fraction of Shackleton material. Generally, higher emplacement speeds result in greater mixing; however, the influence of emplacement angle and surface slopes on the degree of mixing remains to be investigated in more detail. In particular, it is unclear whether enhanced mixing occurs under conditions of higher lateral spreading velocities and thus shallower emplacement angles, or whether steeper emplacement angles promote mixing by incorporating more local material through more efficient excavation.

However, the uppermost layer of the Shackleton ejecta deposit has been resurfaced by impact gardening since its emplacement in the Imbrian period. Therefore, our mixing factors should be interpreted as first-order constraints on ejecta emplacement and provenance rather than deterministic predictions of sample composition at specific sites. Depending on the exact formational age of Shackleton crater (∼3.43–3.69 Ga; P. D. Spudis et al. 2008; M. T. Zuber et al. 2012; A. R. Tye et al. 2015; D. A. Kring et al. 2021), the top ∼1 m of its ejecta deposit has been overturned by subsequent impact cratering at least once with 99% probability (E. S. Costello et al. 2020). This suggests that the upper layer underwent intense modification and mixing after its formation, resulting in homogenization. These effects are independent of the distance to the Shackleton crater rim, provided that the sample is collected from the ejecta deposit. Therefore, reworked regolith sampled by surface scooping or shallow drilling or trenching may exhibit smaller particle sizes and younger exposure ages, making it a critical consideration for future sampling and analysis of Shackleton ejecta. Drilling several meters deep is required to reach relatively undisturbed ejecta material from the crater because the upper homogenized regolith is likely to be underlain by layers that show evidence of reworking (E. S. Costello et al. 2018).

6. Implications for Future Exploration and Surface Activities

Multiple landing sites have been suggested in the vicinity of Shackleton crater. These sites are situated on local topographic highs, such as the Shackleton crater rim or the SDGR. The 16 Artemis candidate landing sites located on the continuous Shackleton ejecta deposit (L. Wueller et al. 2026a) span two Artemis candidate landing regions, the "Peak Near Shackleton" (PNS) and "Connecting Ridge" (CR) regions (NASA 2022b). Additionally, six potential landing sites near Shackleton crater have been proposed for the CE-7 mission (Deep Space Exploration Laboratory 2022). The CE-7 landing site *Shackleton 2* (*S2*) overlaps with site *CR07* (L. Wueller et al. 2026a), landing site *S5* overlaps with site *007* (E. Mazarico et al. 2011; D. A. Kring et al. 2020c), and *S6* overlaps with site *CR06* (L. Wueller et al. 2026a; Figure 8(A)).

Sampling and analysis of materials associated with the Shackleton impact may provide access to material from the underlying SDGR, whose composition and origin are of high scientific interest (e.g., A. J. Gawronska & S. J. Boazman 2025). In general, ejecta emplaced closer to the crater rim likely originates from greater depth (H. J. Melosh 1989). Materials of interest include impact melt rocks and melt breccias suitable for radiometric age dating to test model ages of Shackleton crater (e.g., C. K. Shearer & L. E. Borg 2006), thereby constraining an upper bound age of any volatiles within associated PSRs. In addition, boulder samples may provide clear provenance and insights into subsurface stratigraphy (e.g., S. J. Boazman et al. 2022), including high-albedo PAN lithologies (e.g., S. Yamamoto et al. 2012) that can provide insights into lunar differentiation and magmatic processes (National Research Council 2007). Therefore, we provide an assessment of the topographic effects on the distribution of Shackleton ejecta and, consequently, on the sampling and provenance of surface materials for the proposed CE-7 and Artemis candidate landing sites and their surroundings.

6.1. CE-7 Candidate Landing Sites

Candidate landing sites *S1*, *S2*, and *S6* are located on the SDGR between Shackleton and Henson craters, at distances of ∼3.8, ∼8.3, and ∼9.6 km from the rim, respectively (Figure 8(A)). At all three sites, their locations on local topographic highs resulted in the interception of ballistic ejecta trajectories and ejecta emplacement ∼20% (1.22 km; *S1*), ∼17% (1.49 km; *S2*), and ∼13% (1.53 km; *S6*) closer to the Shackleton crater rim than expected for flat terrain. This effectively increased local Shackleton ejecta thickness beyond the nominal estimates of ∼52 to 63 m (*S1*), ∼23 to 28 m (*S2*), and ∼19 to 23 m (*S6*) derived from scaling relationships (Table 1). At sites *S1* and *S2*, ejecta may have been emplaced at lower velocities of ∼115 and 134 m s^{-1} instead of ∼129 and 149 m s^{-1}, respectively, and at steeper angles than expected for flat terrain (Figure 11(A)), leading to reduced mixing with local regolith during ballistic ejecta emplacement. Consequently, the effective mixing factor may be lower than the estimated 0.19 (*S1*) and 0.24 (*S2*) for flat surfaces (Figure 11(B)), thereby increasing the fraction of Shackleton ejecta available for sampling. The Shackleton ejecta deposit represents the stratigraphically youngest material within the ∼696 to ∼718 m thick post-SPA ejecta sequence (T. Frueh et al. 2025b). Landing site *S6* differs from *S1* and *S2*, as it is positioned on the edge of a topographic high, likely increasing the local ejecta thickness (Figure 10(B)). Downrange slopes surrounding the site lead to shallow ejecta emplacement at an angle of ∼34° and at ∼150 m s^{-1} (∼540 km hr^{-1}), which likely has increased ejecta spreading velocities, allowing greater lateral energy to be retained during spreading and deposition. These conditions likely enhanced mixing with local materials, implying an effective mixing factor of ⩾0.25 (Table 1). Consequently, ejecta materials from diverse regional impact events are potentially accessible near site *S6*. For all three landing sites, surface slopes are generally <15° within 500 m of the proposed sites, although steeper areas exist, particularly on the flanks of the SDGR near Spudis crater. Candidate site *S2* overlaps with Artemis candidate landing site *CR07* (Figure 8(A)) and receives extended sunlight during midsummer periods through 2032 (L. Wueller et al. 2026a). Across the small PSRs in this region investigated by L. Wueller et al. (2026a), volatile accumulation is limited by relatively warm temperatures, although volatiles may be present in the subsurface. Site *S6* overlaps with site *CR06* (Figure 8(A)) and offers illumination conditions and resulting thermal conditions that are challenging for surface operations during the midsummer periods until 2032 (L. Wueller et al. 2026a).

Candidate landing sites *S3* and *S4* lie on the perched rim of Shackleton crater ∼8.5 km apart along the rim crest at elevations of ∼1.5 km and ∼1.4 km, respectively (Figure 8(A)). Scaling relationships that estimate ejecta thickness and mixing have limited applicability on the crater rim (McGetchin et al. 1973; V. R. Oberbeck et al. 1975; V. L. Sharpton 2014). However, numerical modeling of the Shackleton impact event (S. H. Halim et al. 2021) indicates >150 m of ejecta on the rim crest (A. J. Gawronska et al. 2020), slightly exceeding the estimates of ∼122 to 146 m (*S3*) and ∼126 to 151 m (*S4*) derived by scaling relationships (Table 1). Surface materials near both sites likely consist almost entirely of ejecta and structurally uplifted target rock, with <14% contribution from local regolith (Table 1). The ejecta emplaced near the rim was excavated at shallower excavation angles and emplaced at lower velocities than materials emplaced farther away, resulting in minimal mixing (Figure 11). Due to the stratigraphic inversion during crater formation (H. J. Melosh 1989), samples collected in these areas may provide access to deeper stratigraphic units, potentially including material linked to nearby PAN locations identified in spectral data (e.g., S. Yamamoto et al. 2012). However, surface mobility and landing at both sites are restricted to the perched rim segment, which is surrounded by steep slopes >20°, requiring high landing accuracy. At site *S3*

Table 1
Estimated Ejecta Thicknesses and Mixing Factors for the Proposed CE-7 Landing Sites

	Shackleton 1	Shackleton 2	Shackleton 3	Shackleton 4	Shackleton 5	Shackleton 6
Shackleton Ejecta Thickness (m) (T. R. McGetchin et al. 1973)	⩾52.5 (+8.8, −7.5)	⩾23.0 (+7.8, −5.8)	∼121.6 (+1.7, −1.7)	∼126.1 (+1.0, −1.0)	⩾9.2 (+5.2, −3.3)	⩾18.8 (+7.2, −5.2)
Shackleton Ejecta Thickness (m) (V. L. Sharpton 2014)	⩾63.0 (±19.0)	⩾27.6 (±8.3)	∼145.9 (±44.0)	∼151.3 (±45.6)	⩾11.1 (±3.3)	⩾22.6 (±6.8)
Cumulative post-SPA Ejecta Thickness (m) (T. Frueh et al. 2025b)	717.8	688.5	606.4	612.1	820.2	691.4
Relative Emplacement Speed (Figure 9(A))	slower	much slower	slower	slower	slower	much slower
Mixing Factor (V. R. Oberbeck et al. 1975)	⩽0.19	⩽0.24	⩽0.14	⩽0.14	⩽0.31	⩾0.25
Ratio of Local to Shackleton Ejecta Material	decreased (more ejecta)	decreased (more ejecta)	decreased (more ejecta)	decreased (more ejecta)	decreased (more ejecta)	increased (less ejecta)

Note. The signs indicate whether topographic effects result in increased (⩾), decreased (⩽), or nominal (∼) thicknesses or mixing relative to the predictions based on scaling relationships.

Table 2
Estimated Ejecta Thicknesses and Mixing Factors for Identified Artemis Candidate Landing Sites in the "Peak Near Shackleton" Region (L. Wueller et al. 2026a)

	PNS01	PNS02	PNS03	PNS04	PNS05	007
Shackleton Ejecta Thickness (m) (T. R. McGetchin et al. 1973)	⩾16.8 (+6.9, −4.9)	⩾25.8 (+8.1, −6.2)	⩾10.4 (+5.5, −3.6)	⩾12.6 (+6.1, −4.1)	⩾6.2 (+4.1, −2.5)	⩾9.2 (+5.2, −3.3)
Shackleton Ejecta Thickness (m) (V. L. Sharpton 2014)	⩾20.1 (±6.1)	⩾31.0 (±9.3)	⩾12.5 (±3.8)	⩾15.1 (±4.6)	⩾7.5 (±2.3)	⩾11.1 (±3.3)
Cumulative post-SPA Ejecta Thickness (m) (T. Frueh et al. 2025b)	905.9	814.3	825.5	801.1	864.1	820.2
Relative Emplacement Speed (Figure 9(A))	nominal	nominal	slower	slower	nominal	slower
Mixing Factor (V. R. Oberbeck et al. 1975)	∼0.26	∼0.23	⩽0.30	⩽0.28	⩾0.34	⩽0.31
Ratio of Local to Shackleton Ejecta Material	nominal	nominal	decreased (more ejecta)	decreased (more ejecta)	increased (less ejecta)	decreased (more ejecta)

Note. The signs indicate whether topographic effects result in increased (⩾), decreased (⩽), or nominal (∼) thicknesses or mixing relative to the predictions based on scaling relationships.

Table 3
Estimated Ejecta Thicknesses and Mixing Factors for Identified Artemis Candidate Landing Sites in the "Connecting Ridge" Region (L. Wueller et al. 2026a)

	CR01	CR02	CR03	CR04	CR05	CR06	CR07	CR08	001	CRE02
Shackleton Ejecta Thickness (m) (T. R. McGetchin et al. 1973)	⩾42.0 (+8.9, −7.3)	⩾38.1 (+8.8, −7.1)	⩾10.8 (+5.6, −3.7)	⩾7.4 (+4.6, −2.8)	⩾23.1 (+7.8, −5.8)	⩾18.8 (+7.2, −5.2)	⩾23.0 (+7.8, −5.8)	⩾30.6 (+8.5, −6.6)	⩾20.4 (+7.5, −5.5)	⩾8.8 (+5.0, −3.2)
Shackleton Ejecta Thickness (m) (V. L. Sharpton 2014)	⩾50.4 (±15.2)	⩾45.8 (±13.8)	⩾13.0 (±3.9)	⩾8.8 (±2.7)	⩾27.7 (±8.3)	⩾22.6 (±6.8)	⩾27.6 (±8.3)	⩾36.8 (±11.1)	⩾24.4 (±7.4)	⩾10.6 (±3.2)
Cumulative post-SPA Ejecta Thickness (m) (T. Frueh et al. 2025b)	765.1	730.5	641.0	667.4	755.7	691.4	688.5	654.6	693.7	669.8
Relative Emplacement Speed (Figure 9(A))	slo.	slo.	slo.	slo.	slo.	m. slo.	m. slo.	nom.	m. slo.	slo.
Mixing Factor (V. R. Oberbeck et al. 1975)	⩽0.20	⩽0.20	⩽0.29	⩽0.33	⩽0.23	⩾0.25	⩽0.24	∼0.22	⩽0.24	⩽0.31
Ratio of Local to Shackleton Ejecta Material	dec. (m. ej.)	dec. (m. ej.)	dec. (m. ej.)	dec. (m. ej.)	dec. (m. ej.)	inc. (l. ej.)	dec. (m. ej.)	nom.	dec. (m. ej.)	dec. (m. ej.)

Note. The signs indicate whether topographic effects result in increased (⩾), decreased (⩽), or nominal (∼) thicknesses or mixing relative to the predictions based on scaling relationships.

in particular, numerous boulders and rocky craters pose potential operational risks and hazards (S. J. Boazman et al. 2022).

Candidate landing site *S5* is located on the extension of the SDGR near Slater crater atop a local topographic peak that rises ∼1.6 km (Figure 8(A)) and was previously identified and discussed as site *007* by E. Mazarico et al. (2011), D. A. Kring et al. (2020c), N. Kumari et al. (2022), and L. Wueller et al. (2026a). With a distance of ∼15 km, this CE-7 candidate site is the farthest from the Shackleton crater rim. As a result, the estimated Shackleton ejecta deposit is the thinnest among the CE-7 candidate sites, at ∼9 m to 11 m thick (Table 1). Based on the site's location on a topographic peak, ejecta has been emplaced at ∼175 m s^{-1} (∼630 km hr^{-1}), which is ∼5% (∼9 m s^{-1}) slower than in a flat-terrain scenario (Figure 11(A)), with different ejecta spreading velocities between the summit and its slopes. Additionally, the ejected material deposited near site *S5* would have landed ∼1 km (∼7%; +0.47 km/−0.33 km; Table A1) farther from the crater in a flat scenario. Consequently, the local Shackleton ejecta is likely thicker than on flat terrain, as the same ejecta volume has been emplaced over a smaller area. The post-SPA ejecta sequence, with a cumulative thickness of ∼820 m (T. Frueh et al. 2025b), is the thickest among the six CE-7 candidate sites (Table 1). The post-SPA ejecta includes major contributions from the pre-Nectarian-aged Amundsen–Ganswindt basin and the Nectarian-aged Amundsen crater (L. Wueller et al. 2024). Combined with a relatively high mixing factor of 0.31 (Figure 11(B)), this suggests that a variety of ejecta materials are likely to be present near site *S5*. Sampling and age dating diverse clasts could provide valuable constraints on south polar stratigraphy and crustal composition. In addition, landing near site *S5* would benefit from the regionally flat surface slopes of $<10°$, favorable midsummer illumination conditions until 2032, and access to small PSRs that are cold enough to potentially trap and accumulate volatiles (L. Wueller et al. 2026a).

6.2. Artemis Candidate Landing Sites

6.2.1. "Peak Near Shackleton" Region

Candidate landing sites *PNS01* and *PNS02* are characterized by nominal ejecta emplacement velocities and intermediate mixing factors of ∼0.26 and ∼0.23, respectively (Table 2), indicating limited topographic modification of ejecta deposition at these locations. Estimated Shackleton ejecta thicknesses differ notably between the two sites, with *PNS01* yielding ∼17–20 m and *PNS02* yielding ∼26–31 m (Table 2; T.R. McGetchin et al. 1973; V. L. Sharpton 2014). With ∼906 m, the cumulative post-SPA ejecta near site *PNS01* is the thickest in the PNS region (T. Frueh et al. 2025b), potentially containing a stratigraphically diverse record of south polar impact resurfacing.

Artemis candidate sites *PNS03*, *PNS04*, and *007* share reduced ejecta emplacement velocities relative to a flat-terrain scenario (Figure 11(A)) due to their position on local topographic highs that intercept ballistic ejecta trajectories. This results in less lateral transportation and vertical mixing with local materials upon ejecta emplacement, suggesting that the ratio of local material to Shackleton ejecta is decreased relative to flat-terrain predictions of ∼0.30, ∼0.28, and ∼0.31, respectively (Table 2). Consequently, the fraction of Shackleton ejecta available for surface and shallow subsurface sampling may be increased. Estimated Shackleton ejecta thicknesses are comparable across this group of landing sites, ranging from ∼10 to 13 m (*PNS03*), ∼13 to 15 m (*PNS04*), and ∼9 to 11 m (*007*), with topography-controlled local ejecta accumulation suggesting these estimates represent lower bounds (Figure 10(B); Table 2). Landing site *007* (E. Mazarico et al. 2011; D. A. Kring et al. 2020c) overlaps with CE-7 candidate landing site *S5* (see Section 6.1) and thus, ejecta emplaced here would have been emplaced ∼1 km (∼7%; +0.47 km/−0.33 km; Table A1) farther away from Shackleton crater than on flat terrain.

Site *PNS05* is distinct within the PNS region, as nominal ballistic ejecta emplacement speeds combined with shallow emplacement angles likely promoted greater mixing with local materials and lateral spreading of emplaced Shackleton ejecta. This results from the site's location on slopes facing away from Shackleton crater, potentially increasing the fraction of local material beyond the ∼34% estimated for flat surfaces (Table 2; V. R. Oberbeck et al. 1975).

6.2.2. "Connecting Ridge" Region

In the "Connecting Ridge" region, candidate landing sites *CR01*, *CR02*, *CR05*, *CR07*, and *001* share slower relative ejecta emplacement velocities and low to moderate mixing factors ranging from ∼20%–24% (V. R. Oberbeck et al. 1975); although, local topography may have resulted in less mixing, and thus, a higher fraction of Shackleton ejecta may be present for sampling (Table 3). Estimated Shackleton ejecta thicknesses are highest at *CR01* (∼42–50 m) and *CR02* (∼38–46 m), which are situated the closest to the rim of Shackleton crater (Figure 8(A)). Additionally, the local topography may have resulted in even thicker Shackleton ejecta deposits (Table 3). Ejecta near candidate site *001* was emplaced 1.58 km (∼15%; +0.50 km/−0.72 km; Table A2) closer to the Shackleton crater rim and ∼10% slower (∼141 m s^{-1} instead of ∼157 m s^{-1}) than one would expect for a flat pre-impact topography. Landing site *CR07* overlaps with CE-7 candidate site *S2* (see Section 6.1) and benefits from extended sunlight during midsummer periods through 2032 (L. Wueller et al. 2026a).

Candidate landing sites *CR03*, *CR04*, and *CRE02* are the farthest away from Shackleton crater and, thus, have the thinnest Shackleton ejecta deposits with ∼11–13 m (*CR03*), ∼7–9 m (*CR03*), and ∼9–11 m (*CRE02*). However, local ejecta deposits may be thicker than these estimates because of their location in topographically elevated regions (Figure 8(A)). Because ejecta emplacement is slower at these sites compared to flat terrain, and the local slope configuration, mixing of emplaced ejecta with local materials was likely reduced, leading to higher fractions of ejecta (Table 3). However, the mixing factors are comparatively high, with ∼29% (*CR03*), ∼33% (*CR04*), and ∼31% (*CRE02*), implying that diverse materials from multiple regional impact events may be accessible near these sites.

Artemis candidate landing site *CR06* overlaps with CE-7 site *S6* (see Section 6.1) and is characterized by much slower relative emplacement speeds due to its location atop the SDGR (Figure 8(B)). The high topography intercepted ballistic ejecta trajectories, resulting in ejecta deposition 1.53 km (∼13%; +0.86 km/−0.55 km; Table A2) closer to Shackleton crater than estimated by scaling laws that assume flat topography. The estimated Shackleton ejecta thickness of ∼19–23 m and cumulative post-SPA ejecta thickness of ∼691 m are comparable to those of nearby site *CR07*. Due to the site's location on a slope facing away from Shackleton crater, the ejecta emplacement

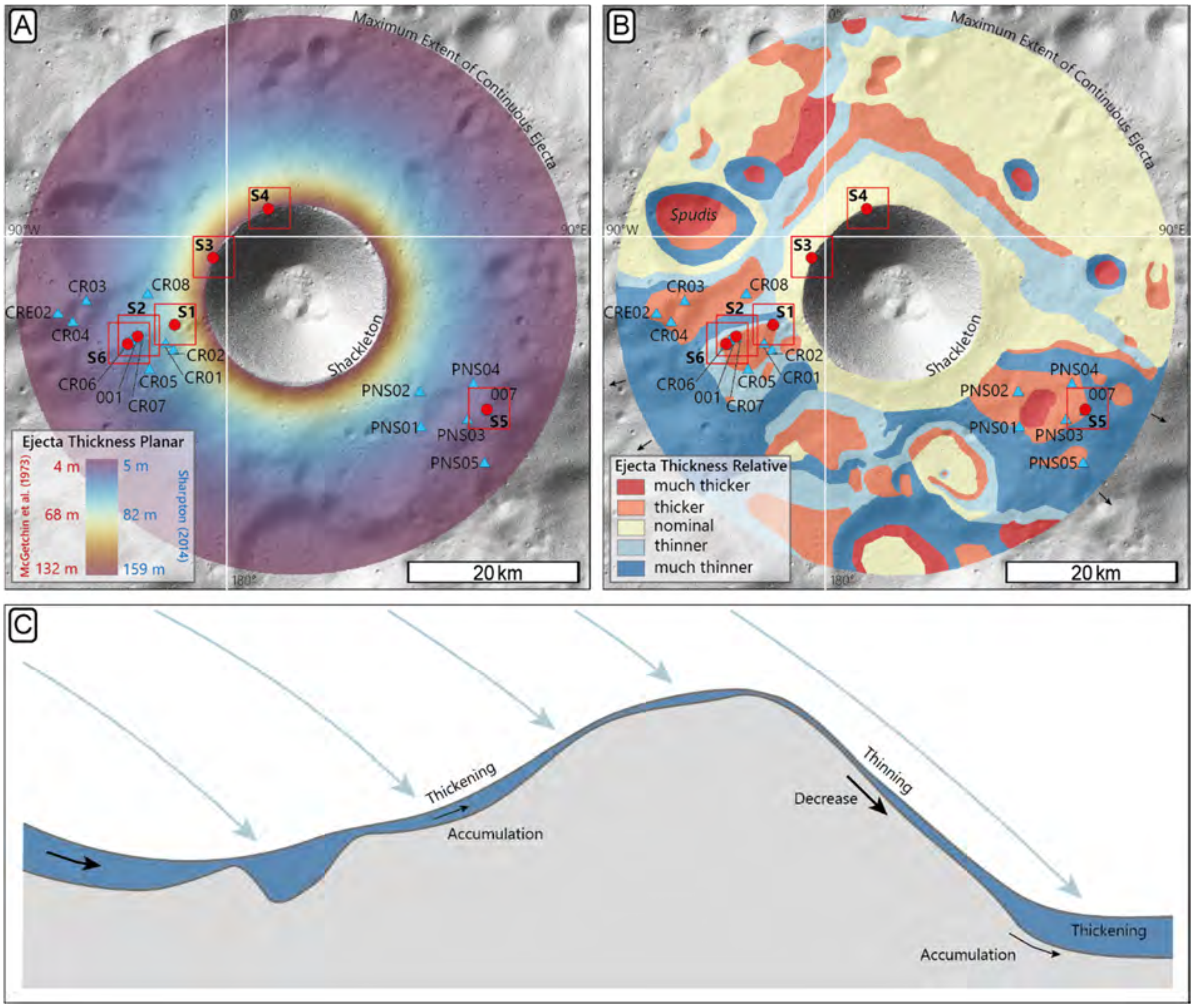

Figure 10. (A) Estimated thickness of Shackleton ejecta on a planar surface (T. R. McGetchin et al. 1973; V. L. Sharpton 2014) on a 20 m pixel^{-1} hillshade map (M. K. Barker et al. 2023). (B) Schematic map qualitatively showing the variation in Shackleton ejecta thickness relative to that predicted by scaling relationships (A), highlighting the influence of regional elevation and slope. It is important to note that in regions with thinner ejecta, the extent of the continuous ejecta deposit is larger. (C) Schematic cross section illustrating the effects of topography on ejecta emplacement, with thickening at the base of steep slopes and thinning on massifs (inspired by a figure from T. Frueh & D. A. Kring 2026a).

angle is shallow with ∼34° (for an ejection angle of 45°). This suggests that mixing at site *CR06* is likely increased, leading to a higher fraction of local materials (Table 3).

Candidate landing site *CR08* is unique within the CR region, as local topography did not affect ejecta velocities and mixing with local material upon emplacement (Table 3). Because of its location, ejecta may have accumulated in this region, potentially resulting in deposits thicker than the estimated ∼31–37 m of Shackleton ejecta and the ∼655 m of cumulative post-SPA ejecta (T. Frueh et al. 2025b; T. R. McGetchin et al. 1973; V. L. Sharpton 2014). Due to the combination of nominal emplacement speed and mixing, this site could serve as a reference for calibrating topographic effects on ejecta emplacement inferred at other landing sites on the continuous ejecta deposit of Shackleton crater.

6.3. Synthesis

Although ejecta thickness and mixing with local materials vary with distance from the Shackleton crater rim and are further modified by topographic effects on ejecta emplacement and deposition, missions targeting these deposits will have access to scientifically promising samples. Consequently, all proposed CE-7 and Artemis landing sites on the Shackleton ejecta deposit (Deep Space Exploration Laboratory 2022; D. A. Kring et al. 2023; L. Wueller et al. 2026a) have the potential to obtain valuable samples and data on lunar impact history and crustal evolution. Surface scooping will likely sample material that has been affected by space weathering, whereas shallow drilling or trenching will likely sample Shackleton ejecta that has been overturned and homogenized by subsequent impact gardening (e.g., E. S. Costello et al. 2020). Deeper subsurface drilling, however, will potentially provide access to more undisturbed ejecta materials. We suggest that, when drilling deeper than the estimated thickness of the Shackleton ejecta, the fraction of material originating from other regional impact events than Shackleton increases. Furthermore, landing anywhere on the continuous ejecta deposit of the Shackleton crater and using a ground-penetrating radar to probe the subsurface, as planned for the CE-7 mission (C. Wang et al. 2024), can provide valuable insights into regional stratigraphy and, potentially, help resolve discrepancies among existing crater scaling models (e.g., T. R. McGetchin et al. 1973; V. L. Sharpton 2014). Additionally, investigating and understanding the processes affecting

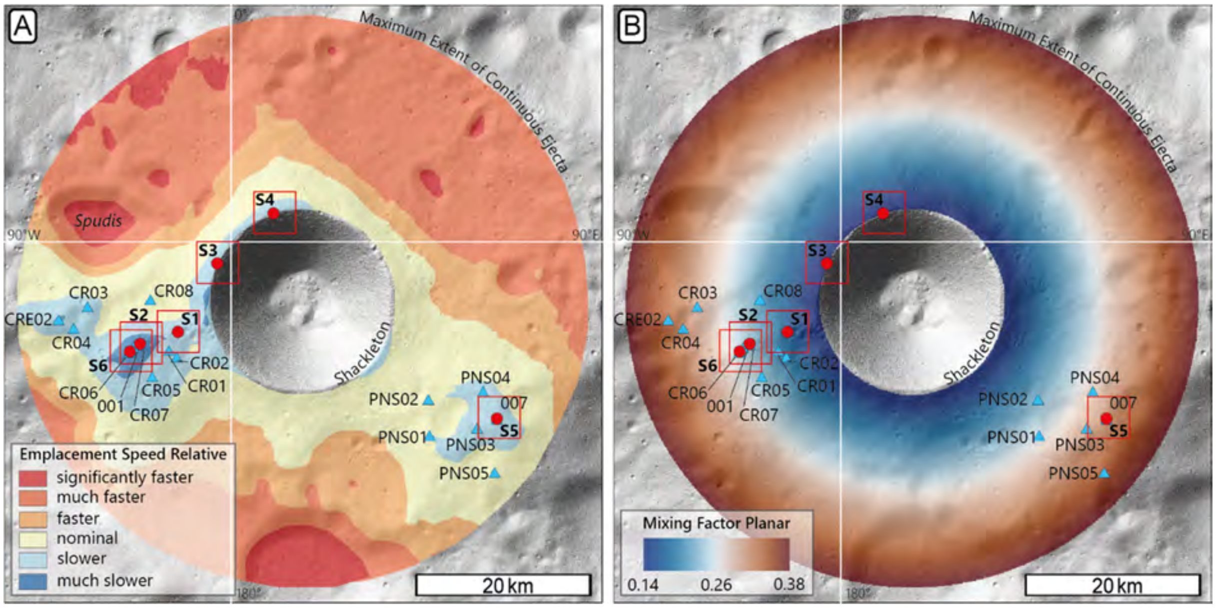

Figure 11. (A) Emplacement speed of Shackleton ejecta relative to a flat-terrain scenario on a 20 m pixel^{-1} hillshade map (M. K. Barker et al. 2023). (B) Estimated mixing factor of local material with ejecta in a planar scenario (V. R. Oberbeck et al. 1975). Mixing increases with distance from the crater.

ejecta distribution and sample provenance remain critical for sample analyses and interpretation to maximize the scientific impact of such missions.

7. Conclusions

The Shackleton crater region records a complex geological history that is central for understanding the evolution of the south polar environment and guiding future exploration. Our geological mapping demonstrates that the region is dominated by pre-Nectarian materials associated with the formation of the SPA basin and subsequent impact events that redistributed SPA and, potentially, underlying crustal materials across the region. The formation of the ∼21 km diameter Shackleton impact during the Imbrian period represents the last major cratering event in the study region. Because the crater formed on the topographically prominent Shackleton-de Gerlache Ridge (SDGR), surrounding topographic variations significantly influenced the emplacement distance, velocity, and angle of Shackleton ejecta. This resulted in locally extended or shortened emplacement distances relative to flat terrain. An assessment of topographic effects on ejecta thickness and mixing with local materials at Artemis and Chang'e-7 (CE-7) candidate landing sites reveals that all sites within the continuous Shackleton ejecta deposit provide access to scientifically valuable samples. Estimated thicknesses of Shackleton ejecta range from ∼6 m at the most distal Artemis landing site (*PNS05*) to ∼150 m at CE-7 landing site *S4* on the crater rim. Ejecta thickness generally decreases with distance from the crater but is locally modified by topography, leading to thicker deposits in topographic lows and thinner deposits on topographic highs or steep surfaces. The topography of the SDGR also controls the mixing of ejecta with local materials upon emplacement, thereby modifying the provenance of samples near potential landing sites. Therefore, it is essential to consider these factors when selecting scientifically promising landing sites, targeting sample materials, and interpreting the provenance of obtained samples.

Data Availability

The final geologic map product and georeferenced Shackleton ejecta maps (Figures 10 and 11) are available via Zenodo, doi:10.5281/zenodo.19691156. The candidate landing sites shown in Figures 2, 8, 10, and 11 (blue triangles) are available from Zenodo (L. Wueller et al. 2026b). The MATLAB script can be accessed via Zenodo (T. Frueh & D. A. Kring 2026b). The post-SPA ejecta thickness can be downloaded from T. Frueh et al. (2025b). The spectral maps can be found in M. Lemelin et al. (2022b).

Acknowledgments

L.W., W.I., and C.v.d.B. are supported by German Aerospace Agency (DLR) grant 50OW2402 for participation in the Lunar Reconnaissance Orbiter (LRO) Camera (LROC) Team. Y.Q. and M.T. are funded by HK RGC General Research Fund 17307025. J.W.H. is a visiting professor at the Institut für Planetologie, Universität Münster.

Conflict of Interest

The authors declare no conflicts of interest relevant to this study.

Appendix

Tables A1 and A2 provide an assessment of ejecta emplacement distances with varying ejection angles for profiles shown in Figure 8.

Table A1
Ejecta Emplacement Distance from the Center of Shackleton Crater for Ballistic Trajectories Shown for Profile A in Figure 8, with Varying Ejection Angles (35°, 40°, 45°, 50°, and 55°)

Trajectory (Counted Outward from Crater Center)	Emplacement Distance Assuming Flat Topography (km)	Emplacement Distance Considering Topography for 45° Ejection (km)	Emplacement Distance Considering Topography for 35° Ejection (km)	Emplacement Distance Considering Topography for 40° Ejection (km)	Emplacement Distance Considering Topography for 50° Ejection (km)	Emplacement Distance Considering Topography for 55° Ejection (km)
			Profile A - West			
1	16.50	17.39	17.78	17.56	17.24	17.12
2	17.40	18.37	18.81	18.57	18.22	18.08
3	18.30	19.39	19.87	19.60	19.21	19.06
4	19.50	20.69	21.18	20.91	20.50	20.34
5	20.70	21.93	22.44	22.16	21.75	21.58
6	22.20	23.46	23.92	23.67	23–27	23.11
7	23.90	25.06	25.52	25.26	24.89	24.74
8	25.90	27.29	27.78	27.52	27.09	26.89
9	28.26	29.60	30.17	29.85	29.39	29.20
10	31.00	32.47	32.99	32.71	32.26	32.07
			Profile A - East			
1	16.50	15.91	15.62	15.78	16.01	16.10
2	17.40	16.84	16.60	16.73	16.93	17.01
3	18.30	17.65	17.39	17.53	17.75	17.84
4	19.50	18.83	18.52	18.69	18.94	19.03
5	20.70	20.10	19.76	19.95	20.21	20.30
6	22.20	21.65	21.45	21.57	21.73	21.80
7	23.90	23.03	22.74	22.89	23.16	23.28
8	25.90	24.86	24.39	24.65	25.03	25.19
9	28.26	27.40	26.95	27.20	27.55	27.68
10	31.00	30.73	30.54	30.66	30.79	30.83

Table A2
Ejecta Emplacement Distance from the Center of Shackleton Crater for Ballistic Trajectories Shown for Profile B in Figure 8, with Varying Ejection Angles (35°, 40°, 45°, 50°, and 55°)

Trajectory (Counted Outward from Crater Center)	Emplacement Distance Assuming Flat Topography (km)	Emplacement Distance Considering Topography for 45° Ejection (km)	Emplacement Distance Considering Topography for 35° Ejection (km)	Emplacement Distance Considering Topography for 40° Ejection (km)	Emplacement Distance Considering Topography for 50° Ejection (km)	Emplacement Distance Considering Topography for 55° Ejection (km)
			Profile B - West			
1	16.50	15.28	14.81	15.06	15.48	15.65
2	17.40	16.10	15.51	15.83	16.32	16.51
3	18.30	16.94	16.32	16.67	17.16	17.34
4	19.50	18.01	17.37	17.72	18.25	18.46
5	20.70	19.12	18.40	18.80	19.39	19.62
6	22.20	20.67	19.81	20.28	20.97	21.22
7	23.90	22.72	21.97	22.41	22.97	23.16
8	25.90	25.25	24.74	25.06	25.39	25.49
9	28.26	28.01	27.83	27.94	28.06	28.10
10	31.00	31.28	31.64	31.49	31.30	31.23
			Profile B - East			
1	16.50	17.06	17.34	17.18	16.96	16.88
2	17.40	18.12	18.46	18.27	17.99	17.89
3	18.30	19.13	19.49	19.29	18.99	18.87
4	19.50	20.40	20.78	20.57	20.26	20.14
5	20.70	21.68	22.10	21.87	21.53	21.39
6	22.20	23.25	23.66	23.44	23.08	22.94
7	23.90	24.92	25.31	25.09	24.76	24.63
8	25.90	26.91	27.36	27.11	26.75	26.61
9	28.26	29.41	29.83	29.60	29.24	29.08
10	31.00	31.97	32.25	32.14	31.83	31.70

ORCID iDs

Lukas Wueller https://orcid.org/0009-0007-6357-3438
Yuqi Qian https://orcid.org/0000-0001-7119-5501
James W. Head https://orcid.org/0000-0003-2013-560X
Carolyn H. van der Bogert https://orcid.org/0000-0003-2882-7037

References

Agarwal, N., Haridas, A., Khanna, N., Srivastava, P., & Jain, V. 2019, Study of Morphology and Degradation of Lunar Craters Using Chandrayaan–1 Data, P&SS, 167, 42

Anderson, J. L. B., Schultz, P. H., & Heineck, J. T. 2003, Asymmetry of Ejecta Flow During Oblique Impacts Using Three-dimensional Particle Image Velocimetry, JGRE, 108, 5094

Archinal, B. A., Weller, L. A., Richie, J. O., et al. 2023, Controlled High-resolution LROC NAC Polar Mosaics, LPICo, 2806, 2333

Barker, M. K., Mazarico, E., Neumann, G. A., et al. 2023, A New View of the Lunar South Pole from the Lunar Orbiter Laser Altimeter (LOLA), PSJ, 4, 183

Bernhardt, H., Robinson, M. S., & Boyd, A. K. 2022, Geomorphic Map and Science Target Identification on the Shackleton-de Gerlache Ridge, Icar, 379, 114963

Bernhardt, H., Walsh, J. M., Schröder, L. M., et al. 2025, Numeric Ring-reconstructions Based on Massifs Favor a Non-oblique South Pole-Aitken-forming Impact Event, E&PSL, 650, 119123

Boazman, S. J., Shah, J., Gawronska, A. J., et al. 2022, The Distribution and Accessibility of Geologic Targets Near the Lunar South Pole and Candidate Artemis Landing Sites, PSJ, 3, 275

Cintala, M. J., Berthoud, L., & Hörz, F. 1999, Ejection-velocity Distributions from Impacts into Coarse-grained Sand, M&PS, 34, 605

Costello, E. S., Ghent, R. R., Hirabayashi, M., & Lucey, P. G. 2020, Impact Gardening as a Constraint on the Age, Source, and Evolution of Ice on Mercury and the Moon, JGRE, 125, e2019JE006172

Costello, E. S., Ghent, R. R., & Lucey, P. G. 2018, The Mixing of Lunar Regolith: Vital Updates to a Canonical Model, Icar, 314, 327

Deep Space Exploration Laboratory 2022, The Chang'e-7 mission launch opportunity announcement (original in Chinese) https://mp.weixin.qq.com/s/EGGNRR4jfK5J8978aH8ing

Du, K., Liu, S., Tong, X., et al. 2026, Quantitative Mineral Maps of the Lunar South Polar Region Derived from the Moon Mineralogy Mapper (M3) Data, JGRE, 131, e2024JE008842

Dundas, C. M., & McEwen, A. S. 2007, Rays and Secondary Craters of Tycho, Icar, 186, 31

Fassett, C. I., Head, J. W., Smith, D. E., Zuber, M. T., & Neumann, G. A. 2011, Thickness of Proximal Ejecta from the Orientale Basin from Lunar Orbiter Laser Altimeter (LOLA) Data: Implications for Multi-ring Basin Formation, GeoRL, 38, L17201

Federal Geographic Data Committee 2006, Planetary Geology Features, FGDC Digital Geographic Standard for Geologic Map Symbolization (US Geological Survey)

Fernandes, V. A., Fritz, J., Weiss, B. P., Garrick-Bethell, I., & Shuster, D. L. 2013, The Bombardment History of the Moon as Recorded by 40Ar-39Ar Chronology, M&PS, 48, 241

Frueh, T., Boyce, M., Camon, A., et al. 2025a, Impact Resurfacing of the Artemis Exploration Zone: Sample locations for Primordial Crust and South Pole-Aitken (SPA) Ejecta, JGRE, 130, e2025JE009050

Frueh, T., Camon, A., Boyce, M., et al. 2025b, Complementary Data for "Impact Resurfacing of the Artemis Exploration Zone: Sample Locations for Primordial Crust and South Pole-Aitken Ejecta," v3, Zenodo, doi: 10.5281/zenodo.17195678

Frueh, T., & Kring, D. A. 2026a, The Concept of Ballistic Shadows and the Effect of Slope on Impact Ejecta Emplacement—Implications for the Exploration of the Lunar South Polar Region, Icar, 459, 117228

Frueh, T., & Kring, D. A. 2026b, Complementary Data for "The Concept of Ballistic Shadows and the Effect of Slope on Impact Ejecta Emplacement – Implications for the Exploration of the Lunar South Polar Region," v2, Zenodo, doi:10.5281/zenodo.20776039

Garrick-Bethell, I., Miljković, K., Hiesinger, H., et al. 2020, Troctolite 76535: A Sample of the Moon's South Pole-Aitken basin?, Icar, 338, 113430

Garrick-Bethell, I., & Zuber, M. T. 2009, Elliptical Structure of the Lunar South Pole-Aitken Basin, Icar, 204, 399

Gawronska, A. J., Barrett, N., Boazman, S. J., et al. 2020, Geologic Context and Potential EVA Targets at the Lunar South Pole, ASR, 66, 1247

Gawronska, A. J., & Boazman, S. J. 2025, Characteristics of the Shackleton-de Gerlache Ridge and Implications for Lunar South Polar Geology and Future Sampling Activities, Icar, 441, 116719

Giuri, B., van der Bogert, C. H., Robinson, M. S., & Hiesinger, H. 2024, Multiple Impact Sources for Light Plains Around the Lunar South Pole, JGRE, 129, e2024JE008605

Green, R. O., Pieters, C., Mouroulis, P., et al. 2011, The Moon Mineralogy Mapper (M3) Imaging Spectrometer for Lunar Science: Instrument Description, Calibration, on-orbit Measurements, Science Data Calibration and on-orbit Validation, JGRE, 116, E00G19

Guo, D., Liu, J., Head III, J. W., & Kreslavsky, M. A. 2018, Lunar Orientale Impact Basin Secondary Craters: Spatial Distribution, Size-frequency Distribution, and Estimation of Fragment Size, JGRE, 123, 1344

Halim, S. H., Barrett, N., Boazman, S. J., et al. 2021, Numerical Modeling of the Formation of Shackleton Crater at the Lunar South Pole, Icar, 354, 113992

Haruyama, J., Matsunaga, T., Ohtake, M., et al. 2008, Global Lunar-surface Mapping Experiment using the Lunar Imager/Spectrometer on SELENE, EP&S, 60, 243

Haruyama, J., Yamamoto, S., Yokota, Y., Ohtake, M., & Matsunaga, T. 2013, An Explanation of Bright Areas Inside Shackleton Crater at the Lunar South Pole other than Water-ice Deposits, GeoRL, 40, 3814

Head, J. W. 1975, Processes of Lunar Crater Degradation: Changes in Style with Geologic Time, Moon, 12, 299

Hiesinger, H., & Head, J. W. 2004, Lunar South Pole-Aitken Impact Basin: Topography and Mineralogy, LPI, 35, 1164

Hiesinger, H., & Tanaka, K. 2020, The Planetary Time Scale, Geologic Time Scale (Elsevier), 443

Hiesinger, H., van der Bogert, C. H., Pasckert, J. H., et al. 2012, New Crater Size-frequency Distribution Measurements of the South Pole-Aitken Basin, LPI, 43, 2863

Hiesinger, H., van der Bogert, C. H., Michael, G., et al. 2023, The Lunar Cratering Chronology, RvGeo, 89, 401

Holsapple, K. A. 1993, The Scaling of Impact Processes in Planetary Sciences, AREPS, 21, 333

Holsapple, K. A., & Schmidt, R. M. 1987, Point Source Solutions and Coupling Parameters in Cratering Mechanics, JGRB, 92, 6350

Hood, L., Deca, J., Li, S., et al. 2026, Magnetic Anomalies Near the Lunar Poles: Effects on Surface Albedo and Water Ice Preservation, LPSC, 57, 1528

Hostrawser, J., & Osinski, G. R. 2025, The Amundsen-Ganswindt Basin: An Overlooked Lunar Peak-ring Basin with Multiple Exploration Opportunities, Icar, 441, 116718

Housen, K. R., Schmidt, R. M., & Holsapple, K. A. 1983, Crater Ejecta Scaling Laws: Fundamental forms Based on Dimensional Analysis, JGRB, 88, 2485

Iqbal, W., Wueller, L., Poehler, C. M., et al. 2026a, Geological Mapping of the South Pole-Aitken (SPA) Basin Region of the Moon, Icar, 459, 117234

Iqbal, W., Frigeri, A., Asch, K., et al. 2026b, Geologic Mapping from the Ocean Floor to Outer Space, NatGe, 19, 493

Jolliff, B. L., Gillis, J. J., Haskin, L. A., Korotev, R. L., & Wieczorek, M. A. 2000, Major Lunar Crustal Terranes: Surface Expressions and Crust-mantle Origins, JGRE, 105, 4197

Joy, K. H., Wang, N., Snape, J. F., et al. 2025, Evidence of a 4.33 Billion Year Age for the Moon's South Pole–Aitken Basin, NatAs, 9, 55

Krasilnikov, S. S., Ivanov, M. A., Head, J. W., & Krasilnikov, A. S. 2023, Geologic History of the South Circumpolar Region (SCR) of the Moon, Icar, 394, 115422

Krasilnikov, A. S., Ivanov, M. A., Krasilnikov, S. S., & Head, J. W. 2024, Stratigraphic Cross-sections, Geologic History, and Provenance of Material at the Candidate Landing Sites of the Artemis Missions, Icar, 420, 116190

Kring, D. A., Barrett, N., Boazman, S. J., et al. 2020a, Artemis III EVA Opportunities Along a Ridge Extending from Shackleton Crater Towards de Gerlache Crater, Science Definition Team for Artemis 2042, Lunar and Planetary Institute, https://www.lpi.usra.edu/announcements/artemis/whitepapers/2042.pdf

Kring, D. A., Barrett, N., Boazman, S. J., et al. 2020b, Artemis III EVA Opportunities in the Vicinity of the Lunar South Pole on the Rim of Shackleton Crater, Science Definition Team for Artemis 2040, Lunar and Planetary Institute, https://www.lpi.usra.edu/announcements/artemis/whitepapers/2040.pdf

Kring, D. A., Bretzelder, J. M., Ganesh, I., et al. 2020c, Artemis III EVA Opportunities on the Lunar Farside Near Shackleton Crater, Science

Definition Team for Artemis 2045, Lunar and Planetary Institute, https://www.lpi.usra.edu/announcements/artemis/whitepapers/2045.pdf
Kring, D. A., Bretzelder, J. M., Ganesh, I., et al. 2020d, Artemis III EVA Opportunities on the Rim of de Gerlache Crater, Science Definition Team for Artemis 2043, Lunar and Planetary Institute, https://www.lpi.usra.edu/announcements/artemis/whitepapers/2043.pdf
Kring, D. A. 2025, Ballistic Shadows that Affect Impact Ejecta Distribution in the Moon's South Polar Region, in European Lunar Symp.
Kring, D. A., Bickel, V. T., van der Bogert, C. H., et al. 2023, Elevation Changes and Slope that May Affect EVA Workload Near Potential Artemis Landing Sites, in IEEE Aerospace Conf., 17
Kring, D. A., Kramer, G. Y., Bussey, D. B. J., et al. 2021, Prominent Volcanic Source of Volatiles in the South Polar Region of the Moon, ASR, 68, 4691
Kumari, N., Bretzfelder, J. M., Ganesh, I., et al. 2022, Surface Conditions and Resource Accessibility at Potential Artemis Landing Sites 007 and 011, PSJ, 3, 224
Lawrence, D. J., Feldman, W. C., Elphic, R. C., et al. 2002, Iron Abundances on the Lunar Surface as Measured by the Lunar Prospector Gamma-ray and Neutron Spectrometers, JGRE, 107, 13
Lemelin, M., Lucey, P. G., & Camon, A. 2022a, Compositional Maps of the Lunar Polar Regions Derived from the Kaguya Spectral Profiler and the Lunar Orbiter Laser Altimeter data, PSJ, 3, 63
Lemelin, M., Lucey, P. G., & Camon, A. 2022b, Compositional maps of the lunar polar regions derived from the Kaguya Spectral Profiler and the Lunar Orbiter Laser Altimeter data, v2, Zenodo, doi:10.5281/zenodo.7108163
Luna, J. W., Iqbal, W., Bernhardt, H., et al. 2024, Planetary Geologic Maps: Essential Tools for Scientific Inquiry and Space Exploration, JGRE, 129, e2024JE008442
Mahanti, P., Li, S., Robinson, M. S., et al. 2025, Episodic Mass Wasting and Exposure of High Reflectance Material within the Shackleton cRater Permanently Shadowed Region, JASS, 42, 85
Maxwell, D. E. 1977, Simple Z Model for Cratering, Ejection, and the Overturned Flap, in Impact and Explosion Cratering: Planetary and Terrestrial Implications, 1003
Mazarico, E., Neumann, G. A., Smith, D. E., Zuber, M. T., & Torrence, M. H. 2011, Illumination Conditions of the Lunar Polar Regions using LOLA Topography, Icar, 211, 1066
McEwen, A. S., & Bierhaus, E. B. 2006, The Importance of Secondary Cratering to Age Constraints on Planetary Surfaces, AREPS, 34, 535
McGetchin, T. R., Settle, M., & Head, J. W. 1973, Radial Thickness Variation in Impact Crater Ejecta: Implications for Lunar Basin Deposits, E&PSL, 20, 226
Melosh, H. J. 1989, Impact Cratering: A Geologic Process (Oxford Univ. Press)
Meyer, H. M., Denevi, B. W., Robinson, M. S., & Boyd, A. K. 2020, The Global Distribution of Lunar Light Plains from the Lunar Reconnaissance Orbiter Camera, JGRE, 125, e2019JE006073
Moore, H. J., Hodges, C. A., & Scott, D. H. 1974, Multiringed Basins—Illustrated by Orientale and Associated Features, LPSC, 5, 71
Moriarty, D. P., & Petro, N. E. 2024, Mineralogical Characterization of the Lunar South Polar Region: 1. The Artemis Exploration Zone, JGRE, 129, e2023JE008266
Moriarty, D. P., & Pieters, C. M. 2018, The Character of South Pole–Aitken Basin: Patterns of Surface and Subsurface composition, JGRE, 123, 729
NASA 2022a, Why Artemis will Focus on the Lunar South Polar Region, Architecture Concept Review 2022, NASA, https://www.nasa.gov/wp-content/uploads/2023/10/acr22-wp-why-lunar-south-polar-region.pdf
NASA 2022b, NASA Identifies Candidate Regions for Landing Next Americans on Moon, https://www.nasa.gov/news-release/nasa-identifies-candidate-regions-for-landing-next-americans-on-Moon/
NASA 2024, NASA Provides Update on Artemis III Moon Landing Regions, https://www.nasa.gov/news-release/nasa-provides-update-on-artemis-iii-moon-landing-regions/
National Research Council 2007, The Scientific Context for Exploration of the Moon (The National Academies Press)
Neukum, G., & Ivanov, B. A. 1994, Crater Size Distributions and Impact Probabilities on Earth from Lunar, Terrestrial-planet, and Asteroid Cratering Data, in Hazards due to Comets and Asteroids, 359, 359
Neumann, G. A., Zuber, M. T., Wieczorek, M. A., et al. 2015, Lunar Impact Basins Revealed by Gravity Recovery and Interior Laboratory Measurements, Sci, 1, e1500852
Oberbeck, V. R. 1975, The Role of Ballistic Erosion and Sedimentation in Lunar Stratigraphy, RvGeo, 13, 337
Oberbeck, V. R., & Aggarwal, H. R. 1977, Topographic Analysis of Lunar Secondary Craters of Copernicus and implications, LPSC, 8, 3521
Oberbeck, V. R., Morrison, R. H., & Hörz, F. 1975, Transport and Emplacement of Crater and Basin Deposits, Moon, 13, 9
Offield, T. W., & Pohn, H. A. 1970, Lunar Crater Morphology and Relative-age Determination of Lunar Geologic Units - Part 2. Applications 69-209, US Geological Survey
Orgel, C., Michael, G., Fassett, C. I., et al. 2018, Ancient Bombardment of the Inner Solar System: Reinvestigation of the "Fingerprints" of Different Impactor Populations on the Lunar Surface, JGRE, 123, 748
Petro, N. E., & Pieters, C. M. 2006, Modeling the Provenance of the Apollo 16 Regolith, JGRE, 111, E09005
Pike, R. J. 1974, Ejecta from Large Craters on the Moon: Comments on the Geometric Model of McGetchin et al, E&PSL, 23, 265
Pöhler, C., van der Bogert, C., Hiesinger, H., Ivanov, M., & Head, J. 2021, Geological Mapping of the South Pole-Aitken Basin Region, EPSC, 15, 646
Qiao, L., Xu, L., Head, J. W., et al. 2024, Geological Evidence for Extensive Basin Ejecta as Plains Terrains in the Moon's South Polar Region, NatCo, 15, 5783
Rivera-Valentín, E. G., Fassett, C. I., Denevi, B. W., et al. 2024, Mini-RF S-band Radar Characterization of a Lunar South Pole–crossing Tycho ray: Implications for Sampling Strategies, PSJ, 5, 94
Robinson, M. S., Brylow, S. M., Tschimmel, M., et al. 2010, Lunar Reconnaissance Orbiter Camera (LROC) Instrument Overview, SSRv, 150, 81
Schultz, P. H., & Gault, D. E. 1985, Clustered Impacts: Experiments and Implications, JGRB, 90, 3701
Sharpton, V. L. 2014, Outcrops on Lunar Crater Rims: Implications for Rim Construction Mechanisms, Ejecta Volumes and Excavation Depths, JGRE, 119, 154
Shoemaker, E. M. 1960, Impact Mechanics at Meteor Crater (Princeton Univ. Press)
Shearer, C. K., & Borg, L. E. 2006, Big Returns on Small Samples: Lessons Learned from the Analysis of Small Lunar Samples and Implications for the Future Scientific Exploration of the Moon, Geoch, 66, 163
Skinner, J. A., Jr., Huff, A. E., Black, S. R., et al. 2022, Planetary Geologic Mapping Protocol—2022, Techniques and Methods 11-B13, US Geological Survey
Smith, D. E., Zuber, M. T., Jackson, G. B., et al. 2010, The lunar Orbiter Laser Altimeter Investigation on the Lunar Reconnaissance Orbiter Mission, SSRv, 150, 209
Spudis, P. D., Bussey, B., Plescia, J., et al. 2008, Geology of Shackleton Crater and the South Pole of the Moon, GeoRL, 35, L14201
Stöffler, D., Knoll, H. D., Marvin, U. B., Simonds, C. H., & Warren, P. H. 1980, Recommended Classification and Nomenclature of Lunar Highland Rocks - a Committee Report, in Proc. Conf. Lunar Highlands Crust, 51
Su, B., Chen, Y., Wang, Z., et al. 2025, South Pole-Aitken Massive Impact 4.25 Billion Years Ago Revealed by Chang'e-6 Samples, NSRev, 12, nwaf103
Takeda, H., Yamaguchi, A., Bogard, D. D., et al. 2006, Magnesian Anorthosites and a Deep Crustal Rock from the Farside Crust of the Moon, E&PSL, 247, 171
Tye, A. R., Fassett, C. I., Head, J. W., et al. 2015, The Age of Lunar South Circumpolar Craters Haworth, Shoemaker, Faustini, and Shackleton: Implications for Regional Geology, Surface Processes, and Volatile Sequestration, Icar, 255, 70
Wang, C., Jia, Y., Xue, C., et al. 2024, Scientific Objectives and Payload Configuration of the Chang'E-7 Mission, NSRev, 11, nwad329
Wang, J., Kreslavsky, M. A., Liu, J., et al. 2020, Quantitative Characterization of Impact Crater Materials on the Moon: Changes in Topographic Roughness and Thermophysical Properties with Age, JGRE, 125, e2019JE006091
Wei, G., Li, X., Zhang, W., et al. 2023, Illumination Conditions near the Moon's South Pole: Implication for a Concept Design of China's Chang'E−7 Lunar Polar Exploration, AcAau, 208, 74
Wilhelms, D. E., Howard, K. A., & Wilshire, H. G. 1979, Geologic map of the south side of the Moon IMAP 1162, US Geological Survey
Wilhelms, D. E., McCauley, J. F., & Trask, N. J. 1987, The geologic history of the moon (US Government Publishing Office)
Wueller, L., Berger, L. M., Christopher, H., et al. 2026a, Assessing Potential Landing Sites with Favorable Illumination and Accessible, Potentially Volatile-rich Permanently Shadowed Regions within Artemis Candidate Landing Regions, JGRE, 131, e2025JE009434
Wueller, L., Iqbal, W., Frueh, T., et al. 2024, Geologic History of the Amundsen Crater Region Near the Lunar South Pole: Basis for Future Exploration, PSJ, 5, 147

Wueller, L., Iqbal, W., Frueh, T., et al. 2025, Geologic History of the Mons Malapert and Mons Mouton Regions Near the lUnar South Pole: Basis for Future Exploration, JGRE, 130, e2025JE009127
Wueller, L., Berger, L. M., Christopher, H., et al. 2026b, Complementary Data for Wueller et al. (2026): Assessing Potential Landing Sites with Favorable Illumination and Accessible, Potentially Volatile-Rich Permanently Shadowed Regions within Artemis Candidate Landing Regions, v1, Zenodo, doi:10.5281/zenodo.17084058
Wueller, L., Iqbal, W., van der Bogert, C. H., & Hiesinger, H. 2026c, The Role of Geological Mapping in Selecting Sites for Future Landing and Exploration Missions, in MAPSIT Meeting, 6025
Yamamoto, S., Nakamura, R., Matsunaga, T., et al. 2012, Massive Layer of Pure Anorthosite on the Moon, GeoRL, 39, L13201
Zuber, M. T., Head, J. W., Smith, D. E., et al. 2012, Constraints on the Volatile Distribution within Shackleton Crater at the Lunar South Pole, Natur, 486, 378